Dependence of Contextual Modulation in Macaque V1 on Interlaminar Signal Flow

Shude Zhu[1], Yu Jin Oh[1], Ethan B. Trepka[1], Xiaomo Chen[1,2], Tirin Moore[1*]

Author affiliations:

[1]Department of Neurobiology and Howard Hughes Medical Institute, Stanford University School of Medicine, Stanford, CA 94305, USA.

[2]Center for Neuroscience, Department of Neurobiology, Physiology, and Behavior, UC Davis, Davis, CA 95618, USA.

***Correspondence:** tirin@stanford.edu

Abstract

In visual cortex, neural correlates of subjective perception can be generated by modulation of activity from beyond the classical receptive field (CRF). In macaque V1, activity generated by nonclassical receptive field (nCRF) stimulation involves different intracortical circuitry than activity generated by CRF stimulation, suggesting that interactions between neurons across V1 layers differ under CRF and nCRF stimulus conditions. Using Neuropixels probes, we measured border ownership modulation within large, local populations of V1 neurons. We found that neurons in single columns preferred the same side of objects located outside of the CRF. In addition, we found that cross-correlations between pairs of neurons situated across feedback/horizontal and input layers differed between CRF and nCRF stimulation. Furthermore, independent of the comparison with CRF stimulation, we observed that the magnitude of border ownership modulation increased with the proportion of information flow from feedback/horizontal layers to input layers. These results demonstrate that the flow of signals between layers covaries with the degree to which neurons integrate information from beyond the CRF.

Introduction

The classical receptive field (CRF) defines the region of the sensory periphery where appropriate stimulation evokes a spiking response in a neuron (Hartline, 1938; Alonso and Chen, 2009). Those evoked responses are largely driven by feedforward inputs from earlier stages of sensory processing. In macaque primary visual cortex (V1), neuronal activity is largely determined by ascending input from the dorsal lateral geniculate nucleus (dLGN) which arrives principally in layers 4Cα and 4Cβ (Hubel and Wiesel, 1972; Hendrickson et al., 1978; Blasdel and Lund, 1983; Callaway, 1998; Callaway, 2004). However, considerable evidence has established that the responses of sensory cortical neurons are also robustly influenced by stimulation concurrently presented outside of the CRF (Allman et al., 1985; Fitzpatrick, 2000; Albright and Stoner, 2002; Roelfsema, 2006; Angelucci et al., 2017). Specifically, whereas stimulation outside of the CRF alone fails to evoke spiking responses, such stimulation nonetheless alters the responses evoked by stimulation within the CRF. In visual cortex, these nonclassical receptive field (nCRF) effects often contribute to the neural correlates of visual perceptual phenomena, such as illusory contours (von der Heydt et al., 1984; Ramsden et al., 2001), visual salience and boundary segmentation (Knierim and van Essen, 1992; Sillito et al., 1995; Yan et al., 2018; Lee et al., 2002; Nothdurft et al., 1999), contour integration (Nelson and Frost, 1985; Kapadia et al., 1995; Li et al., 2006), figure-ground segregation (Lamme, 1995; Zipser et al., 1996; Poort et al., 2012), and border ownership (Zhou et al., 2000; von der Heydt, 2015; von der Heydt, 2023).

In contrast to the feedforward mechanisms underlying the CRF, nCRF effects are thought to be generated either by feedback from neurons with larger CRFs in higher areas (Hupe et al., 1998; Bullier et al., 2001; Bair et al., 2003; Nassi et al., 2013; Chen et al., 2017; Klink et al., 2017; Zhang et al., 2014; Nurminen et al., 2018; Keller et al., 2020; Pak et al., 2020; Vangeneugden et

al., 2019; Gieselmann and Thiele, 2022; Chen et al., 2014; van Kerkoerle et al., 2014), or through intracortical horizontal connections (Adesnik et al., 2012; Chisum et al., 2003; Stettler et al., 2002), or by both (Angelucci and Bressloff, 2006; Schwabe et al., 2006; Ichida et al., 2007; Angelucci et al., 2017; Liang et al., 2017; Self et al., 2013). In contrast to feedforward inputs, feedback and horizontal inputs to V1 both avoid layer 4C and terminate predominantly in superficial (layers 1-3) and deep (layers 5-6) layers (Rockland and Lund, 1983; Rockland and Pandya, 1979; Rockland and Virga, 1989; Anderson and Martin, 2009; Markov et al., 2014; Federer et al., 2021; Gilbert and Wiesel, 1983; Shmuel et al., 2005; Siu et al., 2021). These differences between feedforward and feedback/horizontal circuitry suggest that the flow of signals across V1 layers should covary with the type of visual stimulation.

Newly developed, high-density Neuropixels probes have enabled recordings from a large, dense population of neurons (Jun et al., 2017; Zhu et al., 2024; Trautmann et al., 2025), and dramatically increase the quantity of identifiable functional interactions between pairs of neurons, particularly in non-human primates (Trepka et al., 2022). Recently, this approach was used to recapitulate known circuit properties, such as the pairwise lead-lag relationship between simple and complex cells and the canonical laminar input-output relationship in macaque V1 (Trepka et al., 2022), as well as the visual hierarchy in mouse visual cortical (Siegle et al., 2021; Jia et al., 2022) and subcortical areas (Sibille et al., 2022).

Here, using Neuropixels probes, we recorded the activity of hundreds of neurons simultaneously from single V1 columns in anesthetized macaques during CRF and nCRF stimulation. We leveraged the high yields obtained from different layers to examine the organization and circuitry underlying contextual modulation, specifically border ownership (B_{own}). B_{own} is a form of contextual modulation in which neurons signal the occluding border between the

background and a foreground object using stimulus information beyond the CRF. This function appears to be crucial for natural scene segmentation and object recognition (Nakayama et al., 1995). It has been shown that many neurons in early visual areas, including V1, respond differently to identical edges (borders) of objects when those objects lie at different locations outside the CRFs (Zhou et al., 2000; Franken and Reynolds, 2021; Hesse and Tsao, 2016; Hesse and Tsao, 2023). B_{own} emerges rapidly after visual response onset (Sugihara et al., 2011), yet the relative contributions of feedforward, feedback, and horizontal circuits to B_{own} remain unknown. Also unknown is whether B_{own} is present under anesthesia. Several other types of contextual modulation have been demonstrated in anesthetized animals (Ramsden et al., 2001; Hupe et al., 1998; Bair et al., 2003; Allman et al., 1985; Gilbert and Wiesel, 1990; Nothdurft et al., 1999; Webb et al., 2003; Zarella and Ts'o, 2016; Muller et al., 2003; Henry et al., 2013; Bijanzadeh et al., 2018; although see Lamme et al., 1998) and can involve inter-cortical feedback (Nurminen et al., 2018). Moreover, B_{own} has been shown to occur independently of attention (Qiu et al., 2007; O'Herron and von der Heydt, 2009), and before object shape recognition (Williford and von der Heydt, 2016; Ko and von der Heydt, 2018), suggesting it may not rely on higher cognitive control or object recognition areas. Rather, B_{own} may emerge through pre-attentive, automatic grouping mechanism in low/middle level visual areas, signifying a representation of “proto-objects” in the early visual cortex (von der Heydt, 2015; von der Heydt, 2023; Self et al., 2019).

Results

Classical RF stimulation in single V1 columns

Neuronal activity was recorded from two anesthetized rhesus macaques (M1 and M2, *Macaca mulatta*) using high-density, multi-contact Neuropixels probes (version 3A, IMEC Inc., Belgium) (Figure 1A) (Methods). These animals had no prior experience with awake experiments or exposure to the stimuli used in this study. Neuropixels probes were inserted into the lateral operculum of V1 with the aid of a surgical microscope at angles nearly perpendicular to the cortical surface. Prior to insertion, the probes were coated with a DiI derivative for subsequent histological visualization of the tracks (Methods) (Supplementary Figure S1). Four Neuropixels probe penetrations were made either in the opercular surface (M1, *pen 1-2*, ~4-6° eccentricities) or within the underlying calcarine sulcus (M2, *pen 3-4*, ~6-10° eccentricities) using the programmable channel selection feature of the Neuropixels probe. The boundaries of laminar compartments were estimated by combining current-source density (CSD) measurements and histological data (Figure 1B; Supplementary Figure S1) (Methods) (Zhu et al., 2024; Carr et al., 2025). Each recorded neuron was assigned to one of four laminar compartments, specifically 5/6, 4C, 4A/B, 2/3 (mean thickness: 489, 281, 311, 650 µm, respectively, consistent with previous anatomical (O'Kusky and Colonnier, 1982; Lund, 1973) and CSD (Self et al., 2013; Chen et al., 2017) studies). We measured the responses from a total of 677 visually driven neurons (N = 159, 181, 210, and 127 per recording) to classical receptive field (CRF) stimulation, and 621 neurons (N = 142, 179, 152, and 148 per recording) to nonclassical receptive field (nCRF) stimulation (Methods). As a result of the nearly perpendicular penetrations, the visual CRFs of V1 neurons were largely overlapping across the cortical depth (Figure 1C).

115 During each recording session, neurons were first tested with CRF stimuli consisting of
116 drifting Gabor gratings with 1.5 degrees of visual angle (dva) in diameter, presented at the joint
117 CRF location of simultaneously recorded neurons (Methods). In each of the four recordings,
118 neurons across cortical depth exhibited very similar preferences to grating orientations (Figure
119 1D). The modal pairwise difference in preferred orientation between neurons across layers was
120 near zero (*pen1* = 5°; *pen2* = 5°; *pen3* = 1°; *pen4* = 1°). This result confirmed that our recordings
121 were nearly perpendicular and included neurons predominantly from single orientation columns.
122 Gratings were sized to largely restrict the stimuli within the CRFs of recorded neurons to maximize
123 the extent to which V1 responses were driven in large proportion by feedforward circuitry. In V1,
124 geniculocortical inputs initially drive neurons within layers 4Cα and 4Cβ (Hubel and Wiesel,
125 1972; Hendrickson et al., 1978; Blasdel and Lund, 1983), which then propagate to supragranular
126 and infragranular layers (Callaway, 1998; Callaway, 2004).
127
128 **Nonclassical RF stimulation and border ownership**
129 Within each of the recordings, we also examined the responses of V1 neurons to nCRF stimuli. It
130 is known that neurons in primate visual cortex integrate visual information from far beyond their
131 CRFs (Albright and Stoner, 2002; Allman et al., 1985; Fitzpatrick, 2000; Roelfsema, 2006;
132 Angelucci et al., 2017). One example of contextual modulation is the selectivity of neurons to
133 border ownership (B_{own}). Specifically, neurons in early visual areas respond differently to identical
134 edges (borders) of objects when those objects lie at different locations outside the CRFs (Zhou et
135 al., 2000; Franken and Reynolds, 2021; Hesse and Tsao, 2016; Hesse and Tsao, 2023) (Figure 2).
136 As with other forms of nCRF modulation, B_{own} is thought to emerge either by feedback from higher
137 areas (Craft et al., 2007; Jehee et al., 2007; Layton et al., 2012; Eguchi and Stringer, 2016;

138 Wagatsuma et al., 2021; Mehrani and Tsotsos, 2021) or from horizontal connections within the
139 same area (Zhaoping, 2005; Kogo et al., 2010). In V1, feedback and horizontal inputs arrive
140 principally within supragranular and infragranular layers, i.e., they avoid layer 4 (Rockland and
141 Pandya, 1979; Rockland and Lund, 1983; Rockland and Virga, 1989; Anderson and Martin, 2009;
142 Markov et al., 2014; Federer et al., 2021; Gilbert and Wiesel, 1983; Shmuel et al., 2005; Siu et al.,
143 2021). Thus, V1 activity generated by nCRF stimulation is known to involve different circuits
144 compared to the activity generated by CRF stimulation.

145 In this study, border ownership test stimuli consisted of uniformly white or black objects
146 (squares, 8 x 8 dva) on a black or white background, respectively, as in previous studies (Zhou et
147 al., 2000) (Methods). One border of the object fell within the CRFs of the recorded neurons. Within
148 the CRF, the oriented border could either be a dark-light edge or light-dark edge, resulting in two
149 different local contrast polarity (LC) conditions (Figure 2A). Outside the CRF, the stimulus
150 configuration differed for the same LC condition such that the oriented border could belong to
151 opposite sides of an object relative to the CRF. Crucially, across these two object side conditions,
152 the stimulus falling within the CRF was identical (Figure 2B) and was identical within an area that
153 extended well beyond the CRF (8 x 16, dva). In this stimulus configuration, differences in evoked
154 responses between the two object side conditions signify selectivity to border ownership (Zhou et
155 al., 2000). The statistical significance was determined by a two-factor ANOVA on the mean spike
156 counts for each condition, with object side (Side 1 and Side 2) and local contrast (LC1 and LC2)
157 as the factors, along with their interaction (Methods).

158 We observed neurons with B_{own} in our recordings from macaque V1. Figures 2C and 2D
159 shows examples of four neurons selective to B_{own}. Each of these neurons exhibited a preference
160 for LC, with two neurons preferring one contrast polarity and two preferring the other. In addition,

each neuron responded differently depending on which side of the object appeared relative to the CRF, thus exhibiting B_{own}. Three of the neurons responded more vigorously to borders belonging to the lower-left side of object (Side 1) ($p < 10^{-14}$, 10^{-10}, 10^{-3} for neurons 1, 2, and 4, respectively), while one neuron responded more vigorously to the border belonging to the upper-right side of the object (Side 2) ($p = 0.014$, neuron 3). Furthermore, one of the neurons showed a consistent preference for Side 1 across both LCs (neuron 4).

To quantify the B_{own}, as in previous studies (Zhou et al., 2000), we calculated a B_{own} modulation index, defined as the difference in neuronal responses to borders belonging to opposite sides of objects, normalized by the maximum response for each neuron (Methods). Responses to the same side of object, but under opposite LC conditions, were averaged together to control for global luminance differences in the overall display. Across the 621 neurons recorded in four sessions, we found that 133 neurons (21.4% overall; *pen1* = 28.2%; *pen2* = 27.9%; *pen3* = 18.4%; *pen4* = 8.4%) responded differently to identical borders yet belonging to opposite sides of the object, a proportion consistent with previous studies in awake monkeys (Zhou et al., 2000). Neurons with B_{own} were found within all cortical laminar compartments, including input layer 4C (5/6: 28/144 = 19.4%; 4C: 48/212 = 22.6%; 4A/B: 19/114 = 16.7%; 2/3: 28/99 = 28.3%) (Table S1), and the proportion was independent of laminar compartment ($\chi^2(3) = 4.78$, $p = 0.19$, chi-square test of homogeneity). Of all V1 neurons, 96 (15.5%) exhibited B_{own} depending on the LC (5/6: 11.1%; 4C: 17.9%; 4A/B: 14.0%; 2/3: 20.2%), while 37 (6.0%) showed significant effects independent of local contrast (5/6: 8.3%; 4C: 4.7%; 4A/B: 2.6%; 2/3: 8.1%). Thus, the majority of V1 neurons with B_{own} exhibited selectivity for only one local contrast, and neurons with B_{own} invariant to local contrast were rare, also consistent with previous observations (Zhou et al., 2000).

184 **Columnar organization of border ownership selectivity**

185 We next considered whether neurons with B_{own} comprised a distinct group, or instead reflected a
186 general tendency of neurons to prefer one side of the object, with statistically significant neurons
187 falling at the tails of the distribution. We leveraged the large number of simultaneously recorded
188 single neurons to measure the distribution of B_{own} modulation across laminar compartments in
189 each session. We found that in each of the four recordings, the distributions of B_{own} modulation
190 generally appeared unimodal, with neurons exhibiting B_{own} falling at the distribution tails (Figure
191 2E). Surprisingly, we also found that within individual recordings, neurons across the cortical
192 depth tended to share similar preferences for the side of the object. That is, for each recording, the
193 B_{own} modulation index differed significantly from 0 (Median modulation index: *pen1* = 0.14, $p <$
194 10^{-12}; *pen2* = 0.08, p = 0.04; *pen3* = -0.18, $p < 10^{-15}$; *pen4* = 0.10, $p < 10^{-5}$, sign test against zero-
195 median). For example, the first recording (*pen1*) was performed in a column in which most neurons
196 preferred an orientation of 135°. In addition, within that column, neurons tended to exhibit higher
197 responses to a border when it belonged to the lower-left side of an object (side 1), as opposed to
198 the upper-right side (side 2). Thus, V1 exhibited a continuum of B_{own}, and neurons within single
199 columns tended to prefer the same side of objects located outside of the CRF.

200

201 **Interlaminar cross-correlations among neurons within single V1 columns**

202 The large number of simultaneously recorded neurons from each session also allowed us to
203 measure interlaminar information flow among single neurons under different visual stimulation
204 conditions. Temporally precise cross-correlations in spike trains offer a unique means of assessing
205 functional interactions among neurons in neural circuits (Perkel et al., 1967). Cross-correlations
206 can be interpreted as suggesting one of myriad putative circuit arrangements among neuronal

ensembles (Moore et al., 1970; Aertsen and Gerstein, 1985; Melssen and Epping, 1987; Ostojic et al., 2009). The identification of such interactions has played an important role in elucidating neural circuits in the mammalian visual system (Ts'o et al., 1986; Schwarz and Bolz, 1991; Reid and Alonso, 1995; Alonso et al., 1996; Alonso and Martinez, 1998; Usrey et al., 1998; Nelson et al., 1992; Briggs et al., 2013; Roe and Ts'o, 1999; Senzai et al., 2019; Denman and Contreras, 2014; Siegle et al., 2021; Jia et al., 2022; Trepka et al., 2022; Smith and Kohn, 2008; Sibille et al., 2022). In particular, it has been useful in specifying the flow of signals through local neural circuits (Trepka et al., 2022) and distributed networks (Siegle et al., 2021; Jia et al., 2022; Sibille et al., 2022). Notably, past studies have demonstrated that neuronal cross-correlations are dynamic and can depend on stimulus context and behavioral variables (Hembrook-Short et al., 2019; Martin and von der Heydt, 2015; Hung et al., 2007; Hirabayashi and Miyashita, 2005; Hirabayashi et al., 2010; Steinmetz et al., 2000).

Given that V1 activity generated by nCRF stimulation is thought to involve different circuitry than activity generated by CRF stimulation (Angelucci et al., 2017), we next asked if the pattern of cross-correlations measured under classical and nonclassical stimulus conditions might differ in a manner consistent with models of their underlying circuitry. Specifically, modulation of visual responses during nCRF stimulation, such as border ownership stimuli, is thought to emerge from either feedback from higher areas or horizontal connections within the same areas (Bair et al., 2003; Bullier et al., 2001; Hupe et al., 1998; Chen et al., 2017; Gieselmann and Thiele, 2022; Keller et al., 2020; Klink et al., 2017; Nassi et al., 2013; Nurminen et al., 2018; Angelucci et al., 2017; Angelucci and Bressloff, 2006; Ichida et al., 2007; Schwabe et al., 2006; Pak et al., 2020; Vangeneugden et al., 2019; Zhang et al., 2014; Adesnik et al., 2012; Chisum et al., 2003; Stettler et al., 2002; Liang et al., 2017; Craft et al., 2007; Jehee et al., 2007; Chen et al., 2014; Self

et al., 2013; van Kerkoerle et al., 2014), both arriving principally in superficial (layers 1-3) and deep (layers 5-6) layers (Rockland and Lund, 1983; Rockland and Pandya, 1979; Rockland and Virga, 1989; Markov et al., 2014; Federer et al., 2021; Anderson and Martin, 2009; Gilbert and Wiesel, 1983; Shmuel et al., 2005; Siu et al., 2021). In contrast, CRF responses are driven predominantly by feedforward circuitry and geniculocortical inputs to layers 4C (Hubel and Wiesel, 1972; Hendrickson et al., 1978; Blasdel and Lund, 1983; Callaway, 1998; Callaway, 2004). This suggests that the pattern of cross-correlations among neurons across V1 layers may differ under CRF and nCRF stimulus conditions.

Across recording sessions, we calculated cross-correlograms (CCGs) from all possible pairwise combinations of neuronal spike trains during both CRF (Gabor gratings) and nCRF (border ownership) stimulation conditions. Figure 3A shows an example recording session (M1, *pen1*) in which 159 visually responsive neurons were recorded during CRF stimulation, and CCGs were computed for 7,956 pairwise combinations of neurons (Methods). CCGs were determined to be significant if the jitter-corrected CCG peak occurred within 10ms of zero-time lag, and exceeded 7 standard deviations (SD) above the mean of the noise distribution (Siegle et al., 2021; Trepka et al., 2022) (Methods). In this recording, 13.8% of the total CCGs computed were found to be significant. Eight significant pairs are highlighted in Figure 3A, with their corresponding CCGs shown in Figure 3B. The peak lag (PL), defined as the relative time delay in occurrence of peak correlation between two spike trains, was restricted to within 10ms. This metric approximates the synchrony and/or the direction of information flow between neuronal pairs (Aertsen and Gerstein, 1985; Moore et al., 1970; Melssen and Epping, 1987; Ostojic et al., 2009). These examples illustrate the tendency of CCGs to corroborate the circuitry within V1 columns under CRF conditions in that 1) PLs generally increase with larger distances between pairs, and 2) layer

253 4 neurons tend to lead superficial neurons (Trepka et al., 2022). We exploited this latter point to
254 test the extent to which the sequence of information flow across layers differs between CRF and
255 nCRF conditions.
256
257 **Comparison of cross-correlations during CRF and nCRF stimulation.**
258 From the 677 and 621 neurons recorded across the 4 recording sessions during CRF and nCRF
259 stimulation, there were 41,759 and 28,430 pairwise combinations included, respectively
260 (Methods). Of those, we found that 6,937 (16.6%) and 4,826 (17.0%) of the CCGs were significant
261 (CRF: *pen1*: 1099/7956 = 13.8%, *pen2*: 2402/11431 = 21.0%, *pen3*: 2174/17780 = 12.2%, *pen4*:
262 1262/4592 = 27.5%; nCRF: *pen1*: 447/2473 = 18.1%, *pen2*: 2750/11823 = 23.3%, *pen3*: 839/6998
263 = 12.0%, *pen4*: 790/7136 = 11.1%). Notably, the proportion of significant connections were nearly
264 identical under the two stimulus conditions, and also were within the range observed in previous
265 studies of macaque V1 (Chu et al., 2014; Hembrook-Short et al., 2019; Smith and Kohn, 2008;
266 Kohn and Smith, 2005).
267 As noted above, modulation of visual responses during nCRF stimulation, such as border
268 ownership stimuli, is thought to be generated principally by feedback/horizontal connections
269 arriving within superficial and deep layers, which contrasts with feedforward input driving CRF
270 stimulation (Figure 3C). Thus, we asked whether cross-correlations between pairs of neurons
271 situated across laminar compartments depended on the type of visual stimulation. We focused our
272 analysis on CCGs computed from pairs of neurons in which one neuron was located within laminar
273 compartments receiving feedback/horizontal inputs (FH_i), namely layers 2/3 and 5/6, and the other
274 was located within compartments relatively devoid of those inputs, namely 4C and 4A/B. This
275 analysis compared the relative spike timing between neuronal pairs during CRF and nCRF

stimulation. If indeed FH_i contribute more to activity during the latter than the former, then we should expect this to be reflected in lead-lag relationships of the CCGs.

A comparison of V1 CCGs from key interlaminar neuronal pairs during CRF and nCRF stimulation is shown for an example recording session (M1, *pen1*) in Figure 3D. During CRF stimulation, the timing of spikes within compartments 4C and 4A/B generally preceded, or was simultaneous with, spikes within FH_i compartments (CRF: 4C-2/3$_{PL}$ = 2ms, $p < 10^{-7}$; 4A/B-2/3$_{PL}$ = 2ms, $p < 10^{-28}$; 4C-5/6$_{PL}$ = 0ms, p = 0.52; 4A/B-5/6$_{PL}$ = 0ms, p = 0.64; Sign test against zero-median). In contrast, during nCRF stimulation, relative spike timing was shifted in favor of neurons in FH_i compartments. Specifically, during nCRF stimulation, the timing of spikes within compartments 4C and 4A/B lagged or was simultaneous with, spikes within FH_i compartments (nCRF: 4C-2/3$_{PL}$ = 0ms, p = 0.80; 4A/B-2/3$_{PL}$ = 0ms, p = 0.70; 4C-5/6$_{PL}$ = -2.5ms, p = 0.11; 4A/B-5/6$_{PL}$ = 0ms, p = 0.56; Sign test against zero median). To further quantify the apparent shift in lead-lag relationships, we calculated an asymmetry index for each CCG. The asymmetry index is computed as the difference in the CCG integral on either side of zero-time lag, and summarizes the lead-lag relationship independent of the CCG peak (Jia et al., 2022) (Methods). Consistent with the analyses of PL, we found that CCG asymmetries differed significantly between CRF and nCRF stimulation for each of the interlaminar comparisons. In each case, the distribution of asymmetries during nCRF stimulation shifted to favor neurons in FH_i laminar compartments, when compared to CRF stimulation (4C-2/3: CRF_{Asym} = 0.036, $nCRF_{Asym}$ = -0.004, Δ = -0.04, $p < 10^{-6}$; 4A/B-2/3: CRF_{Asym} = 0.046, $nCRF_{Asym}$ = -0.005, Δ = -0.051, $p < 10^{-11}$; 4C-5/6: CRF_{Asym} = -0.010, $nCRF_{Asym}$ = -0.044, Δ = -0.034, p = 0.0015; 4A/B-5/6: CRF_{Asym} = 0.012, $nCRF_{Asym}$ = -0.028, Δ = -0.04, $p < 10^{-5}$; Wilcoxon rank-sum test). Thus, CCG data from this single recording session indicated that

relative spike timing was earlier within FH_i laminar compartments during nCRF stimulation than during CRF stimulation.

Across all recordings, we identified a total of 2,573 and 2,118 significant neuronal pairs from the four interlaminar combinations during CRF (*pen1* = 274; *pen2* = 1187; *pen3* = 560; *pen4* = 302) or nCRF stimulation (*pen1* = 210; *pen2* = 1226; *pen3* = 382; *pen4* = 300), respectively, and compared their CCG asymmetries. Similar to the pattern observed in the example recording, we observed a consistent shift in lead-lag relationships for each of the interlaminar comparisons (Figure 4). Specifically, during nCRF stimulation, the distribution of asymmetries during nCRF stimulation shifted to favor neurons in FH_i laminar compartments, when compared to CRF stimulation (4C-2/3: $CRF_{Asym} = 0.028$, $nCRF_{Asym} = 0.012$, $\Delta = -0.016$, $p < 10^{-9}$; 4A/B-2/3: $CRF_{Asym} = 0.038$, $nCRF_{Asym} = 0.022$, $\Delta = -0.016$, $p < 10^{-9}$; 4C-5/6: $CRF_{Asym} = -0.033$, $nCRF_{Asym} = -0.047$, $\Delta = -0.014$, $p < 10^{-5}$; 4A/B-5/6: $CRF_{Asym} = -0.018$, $nCRF_{Asym} = -0.05$, $\Delta = -0.032$, $p < 10^{-20}$; Wilcoxon rank-sum test). Thus, relative spike timing was earlier within FH_i laminar compartments during nCRF stimulation than during CRF stimulation in the combined dataset, suggesting that the proportion of information flow from FH_i layers to input layers increased during nCRF stimulation. This observation was consistent across individual recording sessions (Table S2). Notably, we observed a similar pattern when instead of asymmetry, we compared CCG peak lags (Supplementary Figure S2A), and when we compared the total number of both significant and nonsignificant pairs (CRF = 15,920; nCRF = 11,263) (Supplementary Figure S2B), and when we compared CCGs with a more stringent significance criterion (10 SDs) in the combined dataset (Supplementary Figure S2C-D).

Lastly, we asked whether interlaminar information flow was related specifically to border ownership modulation, independent of the comparisons between CRF and nCRF stimulation.

321 Since CRF and nCRF stimuli differed in ways potentially unrelated to nonclassical modulation
322 (e.g., variations within the CRF), we sought to assess the extent to which information flow from
323 FH_i to input layers predicted the magnitude of nCRF modulation. To this end, we computed two
324 modulation indices from the same B_{own} test stimuli (Figure 2A), specifically the B_{own} modulation
325 index and the local contrast (LC) index. In contrast to the B_{own} modulation index, which reflects
326 nCRF modulation, the LC index measures selectivity to luminance contrast polarity (dark-light vs.
327 light-dark) within the CRF. We hypothesized that if the relative timing of spiking activity within
328 FH_i laminar compartments is indicative of nCRF modulation, we should expect earlier relative
329 spike timing in FH_i compartments, i.e., lower CCG asymmetries with respect to other
330 compartments, to be associated with greater B_{own}. In contrast, we should not expect that
331 relationship with the LC index.

332 Consistent with our hypothesis, we observed a negative relationship between the B_{own}
333 modulation index and CCG asymmetry across the population and within individual sessions (linear
334 regression: population slope (β) = -0.32, $p < 10^{-27}$; individual sessions: *pen1* = -0.52, $p < 10^{-5}$; *pen2*
335 = -0.06, p = 0.14; *pen3* = -0.25, $p < 10^{-4}$; *pen4* = -0.20, p = 0.008) (Figure 5A). This result suggests
336 that the magnitude of B_{own} modulation for neuronal pairs depended on the proportion of
337 information flow from FH_i compartment to input layers. In contrast, the opposite was true for the
338 LC index. That is, LC index was positively correlated with CCG asymmetry across the population
339 (linear regression: population slope (β) = 0.46, $p<10^{-28}$) (Figure 5B). However, this relationship
340 was not consistent across sessions (individual sessions: *pen1* = -0.30, p = 0.09; *pen2* = 0.33, p <
341 10^{-5}; *pen3* = 0.23, p = 0.006; *pen4* = 0.14, p = 0.04). To explore both results further, we built
342 generalized linear models (GLMs) to assess the dependence of B_{own} or LC modulation on CCG
343 asymmetry to incorporate variations across interlaminar combinations and recording sessions. For

LC modulation, this analysis indicated that the magnitude of LC modulation was not reliably predicted by interlaminar information flow (GLM: coefficient = -0.04, $p = 0.30$; $R^2 = 0.27$) (Table S3). In contrast, for B_{own} modulation, this analysis confirmed that the magnitude of modulation was reliably predicted by interlaminar information flow, independent of variations across interlaminar combinations and recording sessions (GLM: coefficient = -0.16 $p = 1.1*10^{-6}$; $R^2 = 0.11$). These results demonstrate that interlaminar information flow was related specifically to the magnitude of border ownership modulation.

Discussion

We measured the sensitivity of neurons to nCRF stimulation, specifically border ownership, within large, local populations in macaque V1. Consistent with previous studies on awake animals, we observed V1 neurons with border ownership selectivity even under anesthesia. We observed that neurons within single columns tended to prefer the same side of objects located outside of the CRF. In addition, we found that cross-correlations among pairs of neurons situated across FH_i and other laminar compartments differed between CRF and nCRF stimulation. Specifically, neurons within FH_i laminar compartments were more likely to lead pairwise interactions with neurons in other compartments during nCRF stimulation than during CRF stimulation. Moreover, the magnitude of border ownership modulation was predicted by greater information flow from FH_i laminar compartments, independent of the comparisons between CRF and nCRF stimulation. These results demonstrate that the flow of signals between neurons in FH_i and other laminar compartments depends on the degree to which those neurons integrate visual information from beyond the CRF. Below we discuss some potential limitations of the results as well as their implications for the mechanisms underlying contextual modulation.

The observation that neurons within FH_i laminar compartments can lead those in layer 4 during nCRF stimulation may appear surprising. However, several anatomical pathways could mediate the propagation of B_{own} signals from FH_i compartments to layer 4. In macaque V1, layers 5/6 send dense projections to 4A/B (Lund, 1988; Callaway, 1998). In particular, layer 6 pyramidal neurons, especially the subset classified as Type 1 cells, project substantially to layer 4C (Wiser and Callaway, 1996; Fitzpatrick et al., 1985). Projections from layers 2/3 to 4A/B have also been reported (Blasdel et al., 1985; Callaway and Wiser, 1996), and neurons in 4A/B often extend apical dendrites into layers 2/3 (Lund, 1988; Yoshioka et al., 1994). Although direct projections from

374 layers 2/3 to 4C are generally sparse (Callaway, 1998), a subset of neurons in the lower part of
375 layer 3 can give off collateral axons to 4C (Lund and Yoshioka, 1991). Additionally, some 4C
376 neurons extend dendrites into 4B, enabling potential dendritic integration of inputs from more
377 superficial layers (Somogyi and Cowey, 1981; Mates and Lund, 1983; Yabuta and Callaway,
378 1998). Moreover, layers 2/3 may influence 4C neurons disynaptically, without requiring dense
379 monosynaptic connections. Importantly, while CCGs can suggest possible circuit arrangements,
380 functional connectivity may arise through mechanisms not fully captured by traditional anatomical
381 tracing. Our observation of functional inputs from layers 2/3 to layer 4 aligns with prior findings
382 in rodent V1, where CCG analysis (Senzai et al., 2019) or photostimulation (Xu et al., 2016)
383 revealed similar pathways. Nonetheless, future studies will be needed to determine the extent of
384 input to layer 4 neurons from more precise FHi laminae.

385 Each of the laminar compartments designated in this study comprised more than a single
386 distinct anatomical layer. This was done to mitigate the uncertainty in determining exact laminar
387 boundaries, to achieve comparable numbers of neurons across compartments, and to maximize
388 statistical power. In addition, combining layers allowed us to combine feedback with horizontal
389 input layers. It is known that feedback and horizontal connections exhibit layer specificity within
390 superficial and deep layers, e.g., horizontal connections are most prominent in layer 2/3 and 5
391 (Rockland and Lund, 1983; Gilbert and Wiesel, 1983), where feedback connections target
392 primarily in layers 1, upper layer 2, and 5/6 (Rockland and Pandya, 1979; Federer et al., 2021;
393 Shmuel et al., 2005). Yet, they both largely avoid layer 4 (Angelucci et al., 2017). Nonetheless,
394 given that the number of anatomically distinct layers within macaque V1 well exceeds the four
395 designated laminar compartments used here, it is important to consider the extent to which
396 collapsing layers limits the conclusions one can draw from our observations. For example,

397 although layer 6 receives feedback input, it also receives feedforward input directly from the LGN
398 (Hubel and Wiesel, 1972; Hendrickson et al., 1978; Blasdel and Lund, 1983; Callaway, 1998). In
399 addition, layer 4A is generally considered an input layer whereas 4B is not (Callaway, 1998; Hubel
400 and Wiesel, 1972; Blasdel and Lund, 1983; Hendrickson et al., 1978). Thus, the designation of any
401 compartment as nominally input, or feedback was relative and not absolute. That is, superficial
402 (layers 2/3) and deep (layers 5/6) layers receive higher proportions of feedback/horizontal inputs
403 than the 4A/B and 4C compartments. Indeed, previous studies of primate visual cortex have used
404 a similar approach in comparing input and feedback/horizontal laminar compartments (e.g. Hansen
405 et al., 2012; Nandy et al., 2017; van Kerkoerle et al., 2017; Pettine et al., 2019). Thus, the observed
406 changes in pattern of cross-correlations between neurons situated across compartments with
407 different relative feedforward and feedback/horizontal input can be interpreted in light of those
408 input differences.

409 Another important consideration is that a key challenge of studying classical and
410 nonclassical RF effects simultaneously in large neuronal populations is the difficulty in achieving
411 alignment of all CRFs with the test stimuli. Although our probe penetrations were largely normal
412 to the surface and neurons showed minimal deviations in orientation selectivity across the cortical
413 depth, V1 neurons nonetheless exhibit noteworthy RF scatter (location/size) even within single
414 cortical columns (Tootell et al., 1988; Gur et al., 2005; Li et al., 2022). This means that the
415 positioning of stimuli relative to the CRF inevitably varied across simultaneously recorded neurons
416 (e.g., Figure 1C). Moreover, this means that although neurons were generally well driven by CRF
417 grating stimuli and exhibited clear orientation tuning, CRF stimulation was not guaranteed to fall
418 solely within the CRF of all neurons. Nonetheless, involvement of the surround, especially far
419 surround was considerably less extensive for CRF stimulation than for nCRF stimulation.

420 Furthermore, in the latter case, regardless of variability in the CRF location, stimuli falling within
421 the CRF were always matched across nCRF stimulus conditions, and the surrounds were also
422 identical within 8° of the CRF (Figure 2A, B).

423 The experiments described here were performed in anesthetized animals. Several other
424 types of contextual modulation have been demonstrated in anesthetized animals (Ramsden et al.,
425 2001; Hupe et al., 1998; Bair et al., 2003; Allman et al., 1985; Gilbert and Wiesel, 1990; Nothdurft
426 et al., 1999; Webb et al., 2003; Zarella and Ts'o, 2016; Muller et al., 2003; Henry et al., 2013;
427 Bijanzadeh et al., 2018), and can involve inter-cortical feedback (Nurminen et al., 2018).
428 Nonetheless, anesthesia is known to affect certain types of contextual responses in area V1. For
429 example, the "figure-ground segregation" effect, where neurons respond more strongly to a texture
430 in a "figure" region than to the same texture in a "ground" region, has been shown to be suppressed
431 under anesthesia (Lamme et al., 1998) and when figure stimuli are not perceived (Super et al.,
432 2001). However, there has been debate over whether this effect depends on attention and awareness
433 (Marcus and Van Essen, 2002; Jones et al., 2015; Poltoratski and Tong, 2020; Poort et al., 2012;
434 Huang et al., 2020). It is worth noting that in that case, RFs are centered on the figure regions, and
435 the modulation likely involves detecting feature discontinuities around boundaries, followed by
436 region-filling and background suppression. Each step could be influenced differently by behavioral
437 variables. Nevertheless, the center figure enhancement emerges late in the V1 response, ~55ms
438 after response onset (Poort et al., 2012). In contrast, border ownership involves RFs centered on
439 the boundaries, with modulation emerging much earlier at ~10-35ms after response onset
440 (Sugihara et al., 2011). Therefore, although both forms of modulation may involve
441 feedback/horizontal input, the underlying circuitry may differ. Our finding of border ownership
442 modulation in anesthetized animals aligns with previous studies showing that border ownership

modulation can act separately even without attention (Qiu et al., 2007; O'Herron and von der Heydt, 2009) or before object shape recognition (Williford and von der Heydt, 2016; Ko and von der Heydt, 2018), perhaps signifying a representation of "proto-objects" in the early visual cortex through automatic, pre-attentive grouping mechanism (von der Heydt, 2015; von der Heydt, 2023; Self et al., 2019).

Border ownership enables neurons with small CRFs in the early visual cortex to assign the occluding border between image regions to a foreground object, which is crucial for natural scene segmentation and object recognition (Nakayama et al., 1995). Human imaging studies have demonstrated the existence of B_{own} in both lower (Fang et al., 2009) and higher visual areas (Kourtzi and Kanwisher, 2001; Andrews et al., 2002), yet the underlying circuitry is still poorly understood. Several computational models have been proposed to explain B_{own}, including feedforward models (Walker et al., 1999; Sakai and Nishimura, 2006; Super et al., 2010), horizontal models (Zhaoping, 2005; Kogo et al., 2010), and feedback models (Craft et al., 2007; Jehee et al., 2007; Jeurissen et al., 2016). Yet cues for determining B_{own} often lie far from the CRF and beyond the extents of geniculocortical and horizontal V1 connections (Angelucci et al., 2017). Furthermore, conduction along horizontal fibers appears too slow (0.1-0.4 mm/ms) (Grinvald et al., 1994; Bringuier et al., 1999; Girard et al., 2001) to account for the rapid (~10-35ms) emergence of B_{own} and its independence from object size (Zhang and von der Heydt, 2010; Sugihara et al., 2011). In contrast, feedback inputs can be conducted through fibers 10 times faster (20-60 mm/ms) (Girard et al., 2001), even via monosynaptic connections (Siu et al., 2021), and contribute to modulating the early responses of V1 neurons (Hupe et al., 2001; Bair et al., 2003). Thus, although we combined feedback and horizontal recipient layers, the differences in interlaminar signal flow we observed were likely driven predominantly by feedback inputs.

In primates, V1 receives inter-cortical feedback connections primarily from areas V2, V3, V4, MT (Rockland et al., 1994; Markov et al., 2014). Thus, V1 B_{own} signals could be generated via inputs from these areas (Zhou et al., 2000; Hesse and Tsao, 2016; Hesse and Tsao, 2023; Franken and Reynolds, 2021; Zhu et al., 2020). Our results resonate with a recent study reporting that in area V4, B_{own} emerges earliest in deep layers compared to input layers (Franken and Reynolds, 2021). This suggests that the earliest component of B_{own} in V4 is not inherited from feedforward inputs, i.e., from V1/V2, but is generated within deep layers de nova, or through feedback connections that arrive at deep layers (Franken and Reynolds, 2021). This further supports the view that B_{own} in V1 emerges via feedback from higher visual areas. In addition, similar to what we observed in V1, columnar organization of B_{own} was observed in V4 (Franken and Reynolds, 2021). Indeed, neurons with B_{own} are clustered into patches in a wide range of primate visual areas, including area V2, V3, V3A, V4, V4A (Hesse and Tsao, 2023). Thus, the evidence of B_{own} modularity we observed in V1 could arise from organized feedback from the B_{own} modules in those areas. This is supported by recent anatomical evidence suggesting that feedback terminals in V1 are clustered and functionally specific (Angelucci et al., 2002; Federer et al., 2021; Shmuel et al., 2005; Siu et al., 2021).

482 **Figure legends**

483 **Figure 1. Classical receptive field (CRF) stimulation in single V1 columns.**

484 (A) Neuropixels probe (384 channels/3.84mm) penetrations made into the lateral surface or
485 underlying calcarine sulcus of macaque V1. Bottom: Diagram of designated laminar
486 compartments. (B) Current-Source density (CSD) profile from an example recording session (M1,
487 *pen1*), showing the early current sink (red) indicative of layer 4C. Laminar compartment
488 boundaries (dashed lines) were determined using histological data and the CSD profile. (C) Top:
489 71 well-defined classical receptive fields (CRF) vertically stacked along the cortical depth, mapped
490 with a 10 x 10 array (4 x 4 dva) of probe stimuli (gratings, 0.4 dva in diameter). Bottom: Drifting
491 Gabor grating (1.5 dva in diameter) used for CRF stimulation, positioned within the joint receptive
492 fields of recorded neurons. Zero (x, y) denotes the center of the CRF population. (D) Heatmap of
493 visual responses from 159 neurons to 36 drift directions of Gabor gratings, vertically stacked along
494 cortical depth (M1, *pen1*). Top: Distribution of differences in preferred orientation for all pairwise
495 combinations of neurons.

496

497 **Figure 2. Nonclassical receptive field (nCRF) stimulation and border ownership.**

498 (A) Border ownership test stimuli for nCRF stimulation. Stimuli consisted of uniformly white or
499 black objects (8º squares) on black or white backgrounds, respectively. One border of the object
500 fell within the CRFs (red circle) of the recorded neurons, with orientation varying in 45º steps.
501 Within the CRF, depending on local contrast polarity (LC), the border could either be a dark-light
502 edge (LC1, Left column) or a light-dark edge (LC2, Right column). For the same LC condition,
503 the border within the CRF could be the bottom-left edge (Side 1, top row) or top-right edge (Side
504 2, bottom row) of the object. (B) Enlarged view of stimulus configuration within the CRF, showing

identical stimulus regions between Side 1 and Side 2 for each LC condition (8 x 16 dva). (C) Four example B_{own} neurons recorded from V1. For each neuron, dot raster plots (top) and instantaneous firing rates (bottom) show responses to the four stimulus conditions depicted in (A), respectively. Magenta represents Side 1; green represents Side 2. (D) Bar plots showing the mean spike rates of the four neurons across the four stimulus conditions. (E) Top: Cartoon depicting the preferred border orientation for each of the four recording sessions (*pen*1-4). Arrows indicate the preferred side of objects relative to the border in the CRF. Bottom: B_{own} modulation index for each neuron plotted at its recorded cortical depth across the recordings. Color bars on the ordinate represent laminar compartments. Black dots denote statistically significant B_{own} neurons, determined by ANOVA with object side and local contrast as factors ($p < 0.05$). Middle: Marginal distribution of the B_{own} modulation index, red arrows indicating the population median. *$p < 0.05$; ***$p < 10^{-5}$.

Figure 3. Interlaminar cross-correlations during CRF and nCRF stimulation.

(A) Example recording (M1, *pen1*) showing 159 visually responsive neurons (circles) recorded simultaneously during CRF stimulation, plotted at their relative cortical depth. The abscissa is magnified for visualization. Also shown are eight example neuronal pairs with significant CCGs during CRF stimulation. Neuronal pairs with zero-time lag CCGs are connected by dashed lines, while pairs with nonzero-time lag CCGs are connected by arrowed lines, with the arrow pointing to the lagging neuron. (B) Eight corresponding CCGs from (A). Neuronal pairs are separated by their laminar compartment combinations. The reference neuron (1st neuron in the CCG function) is designated as *j*, and the target neuron as *k*. PL (peak lag, ms) is defined as the relative time delay in peak correlation between the two spike trains. (C) Diagram illustrating feedforward and feedback (and horizontal) projections within the designated laminar compartments. Feedforward

528 inputs arrive within laminar compartments 4C, while feedback (and horizontal) projections
529 principally target superficial and deep layers. (D) Heatmap of all significant CCGs during either
530 CRF stimulation (Gabor gratings, top row) or nCRF stimulation (border ownership, middle row),
531 for the four key interlaminar combinations (columns), calculated from one example recording (M1,
532 *pen1*). Individual CCGs are normalized by their absolute maximum for visualization, and different
533 CCGs are vertically stacked. Bottom row: Distribution of CCG asymmetry for each of the four
534 key interlaminar compartments as in (A), across CRF stimulation (gray) and nCRF stimulation
535 (magenta). Arrows indicate the population median. **$p < 0.002$; ***$p < 10^{-5}$.
536
537 **Figure 4. Comparison of interlaminar CCG asymmetries during CRF and nCRF**
538 **stimulation.**
539 Combined dataset for each of the four key interlaminar combinations. Histograms and cumulative
540 distributions of asymmetry for all significant CCGs during CRF (gray) and nCRF (magenta)
541 stimulation. Arrows indicate the population median. ***$p < 10^{-5}$.
542
543 **Figure 5. Dependence of nCRF modulation on interlaminar signal flow.**
544 (A) Scatter plot of the B_{own} modulation index versus CCG asymmetry for all significant CCGs,
545 aggregated across the four key interlaminar combinations and all recording sessions. CCG
546 asymmetries were calculated during nCRF stimulation. The geometric mean of the B_{own} index for
547 each neuronal pair was used. Red lines denote the fitted regression line and the 95% confidence
548 interval in linear regression. (B) Similar to (A), but using the local contrast (LC) index instead of
549 the B_{own} index. The LC index was calculated as the difference in neuronal responses to borders
550 with opposite contrast polarities, normalized by the maximum response.

551 **Supplementary figure legends and tables**

552 **Supplementary Figure S1. Histological data for Neuropixels recordings in macaque V1.**

553 (A) Neuropixels probe (384 channels/3.84mm) penetrations made into the lateral surface or
554 underlying calcarine sulcus of macaque V1. Bottom: Diagram of designated laminar
555 compartments. (B) Histological reconstruction of probe tracks based on DiI derivative staining for
556 two example recordings (*pen3-4*). Here, Neuropixels probes passed through the lateral surface and
557 reached the calcarine sulcus of V1. Only neurons in the calcarine V1 from these two recordings
558 were tested and included in the analysis. Designated boundaries are shown. Scale bar, 500 μm.

559

560 **Supplementary Figure S2. Comparison of interlaminar cross-correlations during CRF and**
561 **nCRF stimulation under different CCG criteria.**

562 (A) Histogram distributions of CCG peak lags for each of the four key interlaminar combinations
563 in the combined dataset during CRF (gray) and nCRF (magenta) stimulation. The shift (Δ) in
564 median CCG peak lags during nCRF stimulation relative to CRF stimulation is shown. Significant
565 CCGs are defined as those with peaks exceeding 7 SD above the noise level (flank). (B) Similar
566 to (A), but comparing CCG asymmetry across all CCGs, including both significant and non-
567 significant ones. (C) Comparison of CCG peak lags using a stricter criterion, where significant
568 CCGs are defined as those with peaks exceeding 10 SD above the noise level (flank). (D)
569 Comparison of CCG asymmetry using the stricter criterion of 10 SD.

Table S1. Number of neurons selective to B_{own} (LC) across recordings.

Layer	Total	p_{Side} <0.05		p_{Side} ≥0.05		Layer	Total	p_{Side} <0.05		p_{Side} ≥0.05	
		p_{LC} ≥0.05	p_{LC} <0.05	p_{LC} <0.05	p_{LC} ≥0.05			p_{LC} ≥0.05	p_{LC} <0.05	p_{LC} <0.05	p_{LC} ≥0.05
	pen1						***pen2***				
2/3	29	6	5	6	12	2/3	55	1	14	18	22
4A/B	19	0	5	8	6	4A/B	34	0	7	10	17
4C	38	3	7	16	12	4C	54	4	15	22	13
5/6	40	2	7	18	13	5/6	27	5	2	4	16
	pen3						***pen4***				
2/3	15	1	1	4	9	2/3	0	0	0	0	0
4A/B	27	0	4	9	14	4A/B	34	3	0	2	29
4C	60	1	12	24	23	4C	60	2	4	5	49
5/6	40	2	7	2	29	5/6	37	3	0	2	32
	pen all										
2/3	99	8	20	28	43						
4A/B	114	3	16	29	66						
4C	212	10	38	67	97						
5/6	144	12	16	26	90						

Table S2. Comparison of CCG asymmetries during CRF and nCRF for each recording.

4C-2/3	*CRF*	*nCRF*	**Δ**	***p***	**4A/B-2/3**	*CRF*	*nCRF*	**Δ**	***p***
pen1	0.036	-0.004	-0.040	$2.8*10^{-7}$	*pen1*	0.046	-0.005	-0.050	$7.5*10^{-12}$
pen2	0.037	0.013	-0.024	$3.7*10^{-9}$	*pen2*	0.030	0.022	-0.008	0.066
pen3	0.017	0.033	0.016	0.29	*pen3*	0.049	0.052	0.003	0.99
4C-5/6	*CRF*	*nCRF*	**Δ**	***p***	**4A/B-5/6**	*CRF*	*nCRF*	**Δ**	***p***
pen1	-0.010	-0.044	-0.033	0.0015	*pen1*	0.012	-0.028	-0.040	$2.1*10^{-6}$
pen2	-0.009	-0.027	-0.018	$1.5*10^{-5}$	*pen2*	-0.011	-0.018	-0.007	0.059
pen3	-0.036	-0.062	-0.026	$5.8*10^{-7}$	*pen3*	-0.025	-0.087	-0.063	$9.1*10^{-15}$
pen4	-0.041	-0.093	-0.051	$3.1*10^{-8}$	*pen4*	-0.030	-0.089	-0.060	$9.1*10^{-12}$

Table S3. GLMs for dependence of border ownership and local contrast on CCG asymmetry.

$$B_{own}(pair) \sim 1 + CCG\ asymmetry + \ laminar\ combination + pen$$

$$LC(pair) \sim 1 + CCG\ asymmetry + \ laminar\ combination + pen$$

GLM	Border ownership (B_{own})				Local contrast (LC)			
	Estimate	SE	tStat	p	Estimate	SE	tStat	p
Intercept	0.166	0.008	21.379	0	0.362	0.010	35.352	0

CCG asymmetry	**-0.158**	0.032	-4.880	**$1.1*10^{-6}$**	**-0.044**	0.043	-1.037	**0.300**
4C-5/6 *rel.4C-2/3*	0.014	0.007	1.948	0.05	-0.117	0.009	-12.606	$3.5*10^{-35}$
4A/B-2/3 *rel.4C-2/3*	$2.5*10^{-5}$	0.006	0.004	0.99	-0.016	0.008	-1.877	0.061
4A/B-5/6 *rel.4C-2/3*	0.009	0.007	1.351	0.18	-0.136	0.009	-15.093	0
pen2 *rel.pen1*	-0.009	0.007	-1.219	0.22	0.010	0.010	0.980	0.327
pen3 *rel.pen1*	0.038	0.009	4.435	$9.7*10^{-6}$	0.035	0.011	3.082	0.002
pen4 *rel.pen1*	0.049	0.010	5.147	$2.9*10^{-7}$	-0.088	0.013	-6.910	$6.4*10^{-12}$

Number of observations: 2118; Error degrees of freedom: 2110

GLM(B_{own}): R^2=0.11; F-statistic vs. constant model: 37.2, p-value=0.

GLM(LC): R^2=0.27; F-statistic vs. constant model: 109, p-value=0.

580 **Methods**

581 *Experimental Model and Subject Details*

582 Anesthetized recordings were conducted in two adult male rhesus macaques (*Macaca mulatta*,
583 M1, 13 kg; M2, 8 kg). All experimental procedures were in accordance with the National Institutes
584 of Health Guide for the Care and Use of Laboratory Animals, the Society for Neuroscience
585 Guidelines and Policies, and with approved Institutional Animal Care and Use Committee
586 (IACUC) protocol (#APLAC-9900) of Stanford University.

587

588 *Electrophysiological Recordings*

589 Prior to each recording session, treatment with dexamethasone phosphate (2 mg per 24 h) was
590 instituted 24 h to reduce cerebral edema. After administration of ketamine HCl (10 mg per
591 kilogram body weight, intramuscularly), monkeys were ventilated with 1-2% isoflurane in a 1:1
592 mixture of N_2O and O_2 to maintain general anesthesia. Electrocardiogram, respiratory rate, body
593 temperature, blood oxygenation, end-tidal CO_2, urine output and inspired/expired concentrations
594 of anesthetic gasses were monitored continuously. Normal saline was given intravenously at a
595 variable rate to maintain adequate urine output. After a cycloplegic agent (atropine sulfate, 1%)
596 was administered, the eyes were focused with contact lenses on an LCD monitor. Vecuronium
597 bromide (60 μg/kg/h) was infused to prevent eye movements.

598 With the anesthetized monkey in the stereotaxic frame, an occipital craniotomy was
599 performed over the opercular surface of V1. The dura was reflected to expose a small (~3 mm^2)
600 patch of cortex. Next, a region relatively devoid of large surface vessels was selected for
601 implantation, and the Neuropixels probe was inserted with the aid of a surgical microscope. Given
602 the width of the probe (70 μm x 20 μm), insertion of it into the cortex sometimes required multiple

603 attempts if it flexed upon contacting the pia. The junction of the probe tip and the pia could be
604 visualized via the (Zeiss) surgical scope, and the relaxation of pia dimpling was used to indicate
605 penetration, after which the probe was lowered at least 3-4 mm. Prior to probe insertion, it was
606 dipped in a solution of the DiI derivative FM1-43FX (Molecular Probes, Inc) for subsequent
607 histological visualization of the electrode track.

608 Given the length of the probe (1 cm), and the complete distribution of electrode contacts
609 throughout its length, recordings could be made either in the opercular surface cortex (M1, *pen* 1-
610 2) or within the underlying calcarine sulcus (M2, *pen* 3-4), by selecting a subset of contiguous
611 active contacts (n = 384) from the total number (n=986). Recordings were made at 1 to 2 sites in
612 one hemisphere of each monkey. At the end of the experiment, monkeys were euthanized with
613 pentobarbital (150 mg/kg) and perfused with normal saline followed by 1 liter of 1% (wt/vol)
614 paraformaldehyde in 0.1 M phosphate buffer, pH 7.4.

615

616 *Visual Stimulation*

617 Visual stimuli were presented at manually mapped receptive field (RF) locations for each
618 recording session on an LCD monitor (Model NEC-4010, dimensions: 88.5 cm (H) x 49.7 cm (V),
619 resolution: 1360 x 768 pixels, frame rate: 60 Hz) positioned 114 cm from the monkeys. RF
620 eccentricities were ~4-6° (M1) and ~6-10° (M2). Visual stimuli were generated using customized
621 MATLAB scripts with the Psychophysics Toolbox extensions (version PTB-3) (Kleiner et al.,
622 2007). A photodiode was used to measure stimulus timing.

623 Classical receptive field (CRF) stimuli consisted of drifting Gabor gratings (2 deg./sec.,
624 100% Michelson contrast) with a diameter of 1.5 degrees of visual angle (dva), positioned within
625 the joint receptive fields (RFs) of recorded neurons. This size was selected to largely constrain the

626 stimuli within the CRFs of recorded neurons, typically ~0.5-1 dva, as determined manually online.
627 Gratings drifted in 36 different directions, from 0 to 360° in 10° steps, in a pseudorandom order.
628 Each stimulus condition was presented for 1 s and repeated 5 or 10 times. A blank screen with
629 equal luminance to the Gabor patch was presented for 0.25 s during the stimulus interval. Stimuli
630 were presented either monocularly (*pen* 1, 3) or both monocularly and binocularly (*pen* 2, 4). Four
631 spatial frequencies (0.5, 1, 2, 4 cycles/deg.) were tested. The optimal eye and spatial frequency
632 conditions were determined offline for further analysis.

633 Nonclassical receptive field (nCRF) stimuli used in this study, i.e., Border ownership test
634 stimuli consisted of uniformly white or black objects (square, 8 x 8 dva) presented on a black or
635 white background, respectively, like previous studies (Zhou et al., 2000). One border of the object
636 fell within the CRFs of the recorded neurons at an orientation that varied in 45º steps. Objects were
637 either 4 x 4 dva or 8 x 8 dva in size, and only conditions with 8 x 8 dva were selected for quantifying
638 border ownership selectivity to tolerate the variation in the CRF locations. Stimuli were presented
639 monocularly to the preferred eye, to avoid the surround stimulating the CRF of the non-preferred
640 eye. For each of the 4 orientation conditions, there were 4 basic conditions (Figure 2A). Within
641 the CRF, the oriented border could either be a dark-light edge or light-dark edge, resulting in two
642 different local contrast (LC) polarity conditions, namely, LC1 and LC2. For the same LC
643 condition, the stimulus configuration outside of the CRF differed such that the oriented border
644 could belong opposite sides of objects, resulting in two different sides of object conditions, namely,
645 side 1 and side 2. Each stimulus condition was presented for 1 s and repeated 10 or 20 times. A
646 blank screen with equal luminance to the mean of object and background luminance was presented
647 for 0.5s during the stimulus interval.
648

Receptive field mapping

In some sessions, the receptive fields of V1 neurons were tested systemically for offline use. CRFs were mapped from a 10 x 10 array (4 x 4 dva) using probe stimuli. The array was centered at the manually determined RFs location. The stimuli consisted of circular sine wave gratings of 0.4 dva in diameter, and 100% Michelson contrast. Gratings were presented at the optimal orientation determined manually online for each recording session and drifted at speed of 2 deg./sec. Each stimulus condition was presented for 0.2s, interleaved with 0.3s of blank screen with equal luminance, and repeated 15 times.

Mean spike counts from 0.05 to 0.25s after each stimulus onset were calculated, resulting in a 10 x 10 matrix containing mean spike rates to each grid location. This 2D matrix was then interpolated to a 40 x 40 matrix (MATLAB function 'interp2') and then smoothed with a 2D Gaussian filter (MATLAB function 'imgaussfilt', σ=2). The outline of the CRF was defined as the contour isoline at 80% of the maximum response using MATLAB function 'contour3'. Neurons with only 1 contour region at the threshold were selected.

Data acquisition and spike sorting

Raw spike-band data were sampled and recorded at 30kHz. They were then median-subtracted and high-pass filtered at 300 Hz during the pre-processing stage. Spike sorting was carried out with Kilosort 3 (Pachitariu et al., 2024) to find spike times and assign each spike to different templates (neurons). Default parameters in Kilosort 3 were used for spike sorting, specifically, Ops.th = [9,9]; Ops.lam = 20; Ops.AUCsplit = 0.8; Ops.ThPre = 8; Ops.sig = 20; Ops.nblocks = 5; Ops.spkTh = -6. The raw sorted data were then manually curated in Phy (*https://github.com/cortex-lab/phy*) to remove templates with very few spikes or with atypical

waveforms and to perform minimal templates merging and splitting. Double-counted spikes from the algorithm fitting the residuals to a new template were identified using established criteria (Siegle et al., 2021), by counting spikes from two templates separated by less than 50μm (~5 channels) and with spike activity occurring within 5 samples (0.167ms). Double-counted spikes from the template smaller in amplitude were removed from further analysis. Visual responsiveness of each unit was assessed under CRF, nCRF, or RF mapping stimulation. For each type of stimulation, a paired-sample t test was performed to determine whether the mean spike counts after each stimulus presentation exceeded the preceding blank period at a significance level of 0.01. Only neurons showing significant visual responsiveness were included for further analysis.

Layer Assignment

The laminar locations of our recorded neurons were estimated based on a combination of functional analysis and histology results (Zhu et al., 2024; Carr et al., 2025). For each recording, we first performed the current source density (CSD) analysis on the stimulus-triggered average of local field potentials (LFP). LFP were low-pass filtered at 200 Hz and recorded at 2500 Hz. LFP signals recorded from every 4 nearby channels were averaged and realigned to the onset of visual stimulus. CSD was estimated as the second-order derivatives of signals along the probe axis using the common five-point formula (Nicholson and Freeman, 1975). The result was then smoothed across space ($\sigma = 120$ μm) to reduce the artifacts caused by varied electrode impedance. We located the lower boundary of the major sink (the reversal point of sink and source) as the border between layer 4C and layer 5/6. We also considered anatomical data in order to localize recorded neurons within gray matter, allowing for minor adjustments (±1 group channel) in layer boundary

694 placement. Subsequent layer boundaries were determined by offsetting the cortical thickness
695 derived from histological slices (Supplementary Fig S1).

696 *Single neuron properties during CRF stimulation*

697 To assess the orientation tuning for each neuron, the spike rates during 0.1 to 1s after each stimulus
698 onset were calculated and averaged for each orientation condition (N= 18). The orientation tuning
699 responses were first smoothed with a Hanning window (half-width at half-height of 20°), and then
700 fitted with a von Mises function (Swindale, 1998)

701 $$y = a_0 + a_1 * e^{a_2*(\cos(2*x-2*a_3)-1)}$$

702 The location of the peak of the fitted curve was determined as the preferred orientation. Only
703 neurons well fit by the function (R^2>0.7) were included for determining pairwise differences in
704 preferences for all combinations in each recording session.

705

706 *Modulation index for border ownership*

707 As in previous studies (Zhou et al., 2000), we calculated a B_{own} modulation index to quantify the
708 selectivity of each neuron for B_{own}. The B_{own} modulation index is defined as

709 $$B_{own}\ index = \frac{0.5 * (R_{LC1} + R_{LC2})_{Side1} - 0.5 * (R_{LC1} + R_{LC2})_{Side2}}{R_{max}}$$

710 Here, $R_{LC,\ Side}$ represents the average spike rate from 0.05 to 0.5 s after stimulus onset for one of
711 four basic conditions, which are derived from the combination of two different *Local Contrast*
712 conditions (LC1 and LC2) and two *Side* conditions (Side 1 and Side 2). Baseline activity was not
713 subtracted. Since the border within the CRF can vary in 45º steps from 0º to 180º, we only selected
714 the optimal orientation for each recording population to calculate the B_{own} index. R_{max} was defined
715 as the maximum response for each neuron across the four basic conditions and four orientations.
716 We used R_{max} instead of summing responses across the four basic conditions to account for the

717 slight variations in orientation preferences among neurons within each recording session. The
718 statistical significance of B_{own} was evaluated using a two-factor ANOVA (MATLAB function
719 'anovan') on the average spike rates for each condition. The two factors were object *Side* (with
720 two levels: Side 1 and Side 2) and *Local Contrast* (with two levels: LC 1 and LC2), including their
721 interactions. A significance level of 0.05 was used. Neurons were considered to exhibit significant
722 B_{own} modulation if they showed a significant main effect for the object *Side* factor. Whether they
723 were invariant to local contrast was determined by the main effect of the *Local Contrast* factor.
724
725 *Cross-correlograms (CCGs)*
726 To measure correlated firing, we computed the cross-correlations between spike trains of
727 all pairs of simultaneously recorded neurons. For each recording session, we calculated cross-
728 correlograms (CCGs) from pairwise combinations of neuronal spike trains during either CRF
729 (Gabor gratings) or nCRF (border ownership) stimulation conditions, respectively. We only
730 included neuronal pairs with geometric mean firing rates more than 0.5 spikes/sec for further
731 analysis. For both conditions, we focused on the spiking activity within the 0.25 -1s window during
732 each stimulus presentation, to mitigate the influence of the transient visual response after stimulus
733 onset. The CCG function for a given pair of neurons was defined as follows:

734 $$CCG(\tau)_{j-k} = \frac{\frac{1}{M}\sum_{i=1}^{M}\sum_{t=1}^{N-\tau} x_j^i\,(t) \times x_k^i(t+\tau)}{\theta(\tau)\sqrt{\lambda_j\lambda_k}}$$

735 where j denotes the first/reference neuron and k denotes the second/target neuron in the CCG
736 function. τ is the time lag between the two spike trains x_j^i and x_k^i from neuron j and k, during trial
737 i. The value of $x_j^i(t)$ and $x_k^i(t)$ is 1 if there is a spike at time bin t and is zero otherwise. M is the
738 total number of trials; N is the number of time bins within a trial. $\theta(\tau) = N - |\tau|$, is a triangular

function that corrects for the degree of overlap in the two spike trains at each time lag. λ_j and λ_k are the mean firing rates of neuron *j* and *k* computed over the same bins used to compute the CCG at each time lag. The normalization by the geometric mean of spike rates is commonly used by previous studies to account for the influence of firing rates on the CCG peaks (Bair et al., 2001; Kohn and Smith, 2005).

To correct for correlations due to stimulus-locking or slow fluctuations in the population responses (e.g., gamma-band activity), we computed a jitter-corrected CCG by subtracting a jittered CCG from the original CCG:

$$CCG_{corrected} = CCG_{original} - CCG_{jittered}$$

The jittered CCG ($CCG_{jittered}$) reflects the expected value of CCG computed from all possible jitters of each spike train within a given jitter window (Harrison and Geman, 2009; Smith and Kohn, 2008). The jittered spike train preserves both the PSTH of the original spike train across trials and the spike counts in the jitter window within each trial. As a result, jitter correction removes the correlation between PSTHs (stimulus-locking) and correlation on timescales longer than the jitter window (slow population correlations). Here, a 25-ms jitter window was chosen based on previous studies (Jia et al., 2013; Siegle et al., 2021). Jitter-corrected CCG ($CCG_{corrected}$) was then smoothed with a 5ms kernel [0.05, 0.25, 0.4, 0.25, 0.05] (Kohn and Smith, 2005; Smith and Kohn, 2008) before further analysis.

We classified a CCG as significant if the peak of the jitter-corrected CCG occurred within 10 ms of zero and exceeded 7 standard deviations (SD) above the mean of the noise distribution, similar to previous studies (Siegle et al., 2021). The noise distribution for a CCG was defined as the flanks of the jitter-corrected CCG ($\{CCG(\tau)|100 \geq |\tau| \geq 50\ ms\}$). All analyses presented in the main text involve only significant, jitter-corrected CCGs. In the supplementary material, we

also applied a more stringent criterion, requiring that significant CCG peaks exceed 10 SD above the noise, and a less stringent criterion that includes both significant and non-significant CCGs. These ensure that our results are robust across the choices of threshold (Supplementary Figure S2).

To assess the directionality of functional interactions or signal flow between pairs of neurons, we focused on two metrics derived from the CCG functions. One is the peak lag (PL), which describes the time lag of peak correlation between the spike trains of neuron *k* (target) relative to neuron *j* (reference). PL is positive if the reference neuron *j* leads target neuron *k* in spike timing, negative if *j* lags *k*, and zero if j and k fire synchronously. The second metric we used to assess the signal flow is CCG asymmetry, computed by subtracting the sum of CCG values during the [-13, 0] ms time window from the sum of CCG values during the [0, 13] ms. Similar to PL, a positive CCG asymmetry indicates that reference neuron *j* leads *k*, while a negative asymmetry indicates that *j* lags *k*. The 13ms window was chosen as half of the 25ms jitter window, consistent with previous studies (Jia et al., 2022). Compared to peak lag, CCG asymmetry additionally captures the strength of the functional interactions between pairs of neurons and is less dependent on the exact shape of the CCG peak, which is often more complex in corticocortical functional interactions (Alonso and Martinez, 1998).

Relationship between B_{own} modulation and interlaminar signal flow

To determine whether the magnitude of border ownership or local contrast modulation is predicted by interlaminar signal flow during nCRF stimulation, we first performed linear regression (MATLAB, 'fitlm', ordinary least squares) and then built generalized linear models (GLMs) using predictors including CCG asymmetry, interlaminar combinations, and recording sessions. We focused on the four key interlaminar combinations (4C-2/3, 4A/B-2/3, 4C-5/6, 4A/B-

785 5/6), where the latter laminar compartments receive feedback/horizontal inputs (FH_i). Only
786 neuronal pairs with significant CCGs were included as individual samples in the GLM. The
787 resulting GLM equations were:

788 $$B_{own}(pair) \sim 1 + asymmetry + \ laminar\ combination + pen$$

789 $$LC(pair) \sim 1 + asymmetry + \ laminar\ combination + pen$$

790 B_{own} (pair) and LC (pair) were calculated as the geometric mean of the B_{own} and LC indices for the
791 constituent neurons in each pair. Specifically, $B_{own}(pair) = \sqrt{abs(B_{own}(j)) * abs(B_{own}(k))}$,
792 where abs($B_{own}(j)$) and abs($B_{own}(k)$) represent the absolute B_{own} modulation indices for constituent
793 neurons j and k. A similar calculation was performed for LC (pair). CCG asymmetries were
794 calculated from the nCRF stimulation condition where neurons in the input layers were selected
795 as reference neurons and the ones in FH_i compartments were target neurons in the CCG. Additional
796 predictors, including interlaminar combinations and recording sessions, were included in the
797 models to incorporate variations when pooling the dataset.

798

799 *Statistical tests*

800 B_{own} for each neuron was assessed with ANOVA. The proportion of B_{own} neurons within
801 different layers was assessed using chi-squared test of homogeneity. The sign of populational
802 border ownership preferences from individual recording session was tested with sign test. The sign
803 of populational CCG peak lag for a given laminar compartment combination was assessed with
804 sign test. The comparisons of peak lag and CCG asymmetry between CRF and nCRF stimulation
805 condition for each laminar compartment combination were evaluated using Wilcoxon rank-sum
806 tests. The dependence between CCG asymmetry and B_{own} for pair of neurons was assessed using
807 linear regression and GLM.

Acknowledgment

We thank Jonathan C. Horton for extensive help with the recordings and histology, Danielle A. Lopes, Stephen Cital, Shellie Hyde and Sam Baker for technical assistance, Tim Harris and Karel Svoboda for providing the Neuropixels probes. This work was supported by NIH Grant EY029759, Brain and Behavior Research Foundation Grant to X.M.; NIH Grants EY014924, NS116623, and a Ben Barres Professorship to T.M.

Author Contributions

Conceptualization, S.Z., X.C. and T.M.; Investigation, S.Z., X.C. and T.M.; Software, S.Z. and E.T.; Formal Analysis, S.Z. and Y.J.O.; Visualization, S.Z., Y.J.O.; Writing – Original Draft, S.Z. and T.M.; Writing – Review and Editing, S.Z., Y.J.O., E.T., X.C., T.M.; Funding Acquisition, X.C. and T.M.

Declaration of Interests

The authors declare no competing interests.

Data and Code Availability

All raw data generated in this study will be deposited in a public repository upon acceptance and made publicly available prior to publication.

The code developed for data analysis has been deposited to GitHub (https://github.com/szhu-007/Zhu_V1_interlaminar-signal-flow) and is freely available for access.

References

ADESNIK, H., BRUNS, W., TANIGUCHI, H., HUANG, Z. J. & SCANZIANI, M. 2012. A neural circuit for spatial summation in visual cortex. *Nature,* 490**,** 226-31.

AERTSEN, A. M. & GERSTEIN, G. L. 1985. Evaluation of neuronal connectivity: sensitivity of cross-correlation. *Brain Res,* 340**,** 341-54.

ALBRIGHT, T. D. & STONER, G. R. 2002. Contextual influences on visual processing. *Annu Rev Neurosci,* 25**,** 339-79.

ALLMAN, J., MIEZIN, F. & MCGUINNESS, E. 1985. Stimulus specific responses from beyond the classical receptive field: neurophysiological mechanisms for local-global comparisons in visual neurons. *Annu Rev Neurosci,* 8**,** 407-30.

ALONSO, J. & CHEN, Y. 2009. Receptive field. *Scholarpedia,* 4**,** 5393.

ALONSO, J. M. & MARTINEZ, L. M. 1998. Functional connectivity between simple cells and complex cells in cat striate cortex. *Nature Neuroscience,* 1**,** 395-403.

ALONSO, J. M., USREY, W. M. & REID, R. C. 1996. Precisely correlated firing in cells of the lateral geniculate nucleus. *Nature,* 383**,** 815-9.

ANDERSON, J. C. & MARTIN, K. A. 2009. The synaptic connections between cortical areas V1 and V2 in macaque monkey. *J Neurosci,* 29**,** 11283-93.

ANDREWS, T. J., SCHLUPPECK, D., HOMFRAY, D., MATTHEWS, P. & BLAKEMORE, C. 2002. Activity in the fusiform gyrus predicts conscious perception of Rubin's vase-face illusion. *Neuroimage,* 17**,** 890-901.

ANGELUCCI, A., BIJANZADEH, M., NURMINEN, L., FEDERER, F., MERLIN, S. & BRESSLOFF, P. C. 2017. Circuits and Mechanisms for Surround Modulation in Visual Cortex. *Annu Rev Neurosci,* 40**,** 425-451.

ANGELUCCI, A. & BRESSLOFF, P. C. 2006. Contribution of feedforward, lateral and feedback connections to the classical receptive field center and extra-classical receptive field surround of primate V1 neurons. *Prog Brain Res,* 154**,** 93-120.

ANGELUCCI, A., LEVITT, J. B., WALTON, E. J., HUPE, J. M., BULLIER, J. & LUND, J. S. 2002. Circuits for local and global signal integration in primary visual cortex. *J Neurosci,* 22**,** 8633-46.

BAIR, W., CAVANAUGH, J. R. & MOVSHON, J. A. 2003. Time course and time-distance relationships for surround suppression in macaque V1 neurons. *J Neurosci,* 23**,** 7690-701.

BAIR, W., ZOHARY, E. & NEWSOME, W. T. 2001. Correlated firing in macaque visual area MT: time scales and relationship to behavior. *J Neurosci,* 21**,** 1676-97.

BIJANZADEH, M., NURMINEN, L., MERLIN, S., CLARK, A. M. & ANGELUCCI, A. 2018. Distinct Laminar Processing of Local and Global Context in Primate Primary Visual Cortex. *Neuron,* 100**,** 259-274 e4.

BLASDEL, G. G. & LUND, J. S. 1983. Termination of afferent axons in macaque striate cortex. *J Neurosci,* 3**,** 1389-413.

BLASDEL, G. G., LUND, J. S. & FITZPATRICK, D. 1985. Intrinsic connections of macaque striate cortex: axonal projections of cells outside lamina 4C. *J Neurosci,* 5**,** 3350-69.

BRIGGS, F., MANGUN, G. R. & USREY, W. M. 2013. Attention enhances synaptic efficacy and the signal-to-noise ratio in neural circuits. *Nature,* 499**,** 476-80.

BRINGUIER, V., CHAVANE, F., GLAESER, L. & FREGNAC, Y. 1999. Horizontal propagation of visual activity in the synaptic integration field of area 17 neurons. *Science,* 283**,** 695-9.

BULLIER, J., HUPE, J. M., JAMES, A. C. & GIRARD, P. 2001. The role of feedback connections in shaping the responses of visual cortical neurons. *Prog Brain Res,* 134**,** 193-204.

CALLAWAY, E. M. 1998. Local circuits in primary visual cortex of the macaque monkey. *Annu Rev Neurosci,* 21**,** 47-74.

CALLAWAY, E. M. 2004. Feedforward, feedback and inhibitory connections in primate visual cortex. *Neural Netw,* 17**,** 625-32.

CALLAWAY, E. M. & WISER, A. K. 1996. Contributions of individual layer 2-5 spiny neurons to local circuits in macaque primary visual cortex. *Vis Neurosci,* 13**,** 907-22.

CARR, N., ZHU, S., CHEN, X., LEE, K., PERLISS, A., MOORE, T. & CHANDRASEKARAN, C. 2025. Neuropixels reveal structure-function relationships in monkey V1 in vivo. *bioRxiv*.

CHEN, M., YAN, Y., GONG, X., GILBERT, C. D., LIANG, H. & LI, W. 2014. Incremental integration of global contours through interplay between visual cortical areas. *Neuron,* 82**,** 682-94.

CHEN, R., WANG, F., LIANG, H. & LI, W. 2017. Synergistic Processing of Visual Contours across Cortical Layers in V1 and V2. *Neuron,* 96**,** 1388-1402 e4.

CHISUM, H. J., MOOSER, F. & FITZPATRICK, D. 2003. Emergent properties of layer 2/3 neurons reflect the collinear arrangement of horizontal connections in tree shrew visual cortex. *J Neurosci,* 23**,** 2947-60.

CHU, C. C., CHIEN, P. F. & HUNG, C. P. 2014. Tuning dissimilarity explains short distance decline of spontaneous spike correlation in macaque V1. *Vision Res,* 96**,** 113-32.

CRAFT, E., SCHÜTZE, H., NIEBUR, E. & VON DER HEYDT, R. 2007. A neural model of figure-ground organization. *J. Neurophysiol,* 97**,** 4310-4326.

DENMAN, D. J. & CONTRERAS, D. 2014. The structure of pairwise correlation in mouse primary visual cortex reveals functional organization in the absence of an orientation map. *Cereb Cortex,* 24**,** 2707-20.

EGUCHI, A. & STRINGER, S. M. 2016. Neural network model develops border ownership representation through visually guided learning. *Neurobiol Learn Mem,* 136**,** 147-165.

FANG, F., BOYACI, H. & KERSTEN, D. 2009. Border ownership selectivity in human early visual cortex and its modulation by attention. *J Neurosci,* 29**,** 460-5.

FEDERER, F., TA'AFUA, S., MERLIN, S., HASSANPOUR, M. S. & ANGELUCCI, A. 2021. Stream-specific feedback inputs to the primate primary visual cortex. *Nat Commun,* 12**,** 228.

FITZPATRICK, D. 2000. Seeing beyond the receptive field in primary visual cortex. *Curr Opin Neurobiol,* 10**,** 438-43.

FITZPATRICK, D., LUND, J. S. & BLASDEL, G. G. 1985. Intrinsic connections of macaque striate cortex: afferent and efferent connections of lamina 4C. *J Neurosci,* 5**,** 3329-49.

FRANKEN, T. P. & REYNOLDS, J. H. 2021. Columnar processing of border ownership in primate visual cortex. *Elife,* 10.

GIESELMANN, M. A. & THIELE, A. 2022. Stimulus dependence of directed information exchange between cortical layers in macaque V1. *Elife,* 11.

GILBERT, C. D. & WIESEL, T. N. 1983. Clustered intrinsic connections in cat visual cortex. *J Neurosci,* 3**,** 1116-33.

GILBERT, C. D. & WIESEL, T. N. 1990. The influence of contextual stimuli on the orientation selectivity of cells in primary visual cortex of the cat. *Vision Res,* 30**,** 1689-701.

GIRARD, P., HUPE, J. M. & BULLIER, J. 2001. Feedforward and feedback connections between areas V1 and V2 of the monkey have similar rapid conduction velocities. *J Neurophysiol,* 85**,** 1328-31.

GRINVALD, A., LIEKE, E. E., FROSTIG, R. D. & HILDESHEIM, R. 1994. Cortical point-spread function and long-range lateral interactions revealed by real-time optical imaging of macaque monkey primary visual cortex. *J Neurosci,* 14**,** 2545-68.

GUR, M., KAGAN, I. & SNODDERLY, D. M. 2005. Orientation and direction selectivity of neurons in V1 of alert monkeys: functional relationships and laminar distributions. *Cereb Cortex,* 15**,** 1207-21.

HANSEN, B. J., CHELARU, M. I. & DRAGOI, V. 2012. Correlated variability in laminar cortical circuits. *Neuron,* 76**,** 590-602.

HARRISON, M. T. & GEMAN, S. 2009. A rate and history-preserving resampling algorithm for neural spike trains. *Neural Comput,* 21**,** 1244-58.

HARTLINE, H. K. 1938. THE RESPONSE OF SINGLE OPTIC NERVE FIBERS OF THE VERTEBRATE EYE TO ILLUMINATION OF THE RETINA. *American Journal of Physiology-Legacy Content,* 121**,** 400-415.

HEMBROOK-SHORT, J. R., MOCK, V. L., USREY, W. M. & BRIGGS, F. 2019. Attention Enhances the Efficacy of Communication in V1 Local Circuits. *J Neurosci,* 39**,** 1066-1076.

HENDRICKSON, A. E., WILSON, J. R. & OGREN, M. P. 1978. The neuroanatomical organization of pathways between the dorsal lateral geniculate nucleus and visual cortex in Old World and New World primates. *J Comp Neurol,* 182**,** 123-36.

HENRY, C. A., JOSHI, S., XING, D., SHAPLEY, R. M. & HAWKEN, M. J. 2013. Functional characterization of the extraclassical receptive field in macaque V1: contrast, orientation, and temporal dynamics. *J Neurosci,* 33**,** 6230-42.

HESSE, J. K. & TSAO, D. Y. 2016. Consistency of Border-Ownership Cells across Artificial Stimuli, Natural Stimuli, and Stimuli with Ambiguous Contours. *J Neurosci,* 36**,** 11338-11349.

HESSE, J. K. & TSAO, D. Y. 2023. Functional modules for visual scene segmentation in macaque visual cortex. *Proc Natl Acad Sci U S A,* 120**,** e2221122120.

HIRABAYASHI, T. & MIYASHITA, Y. 2005. Dynamically modulated spike correlation in monkey inferior temporal cortex depending on the feature configuration within a whole object. *J Neurosci,* 25**,** 10299-307.

HIRABAYASHI, T., TAKEUCHI, D., TAMURA, K. & MIYASHITA, Y. 2010. Triphasic dynamics of stimulus-dependent information flow between single neurons in macaque inferior temporal cortex. *J Neurosci,* 30**,** 10407-21.

HUANG, L., WANG, L., SHEN, W., LI, M., WANG, S., WANG, X., UNGERLEIDER, L. G. & ZHANG, X. 2020. A source for awareness-dependent figure-ground segregation in human prefrontal cortex. *Proc Natl Acad Sci U S A,* 117**,** 30836-30847.

HUBEL, D. H. & WIESEL, T. N. 1972. Laminar and columnar distribution of geniculo-cortical fibers in the macaque monkey. *J Comp Neurol,* 146**,** 421-50.

HUNG, C. P., RAMSDEN, B. M. & ROE, A. W. 2007. A functional circuitry for edge-induced brightness perception. *Nat Neurosci,* 10**,** 1185-90.

HUPE, J. M., JAMES, A. C., GIRARD, P., LOMBER, S. G., PAYNE, B. R. & BULLIER, J. 2001. Feedback connections act on the early part of the responses in monkey visual cortex. *J Neurophysiol,* 85**,** 134-45.

HUPE, J. M., JAMES, A. C., PAYNE, B. R., LOMBER, S. G., GIRARD, P. & BULLIER, J. 1998. Cortical feedback improves discrimination between figure and background by V1, V2 and V3 neurons. *Nature,* 394**,** 784-7.

ICHIDA, J. M., SCHWABE, L., BRESSLOFF, P. C. & ANGELUCCI, A. 2007. Response facilitation from the "suppressive" receptive field surround of macaque V1 neurons. *J Neurophysiol,* 98**,** 2168-81.

JEHEE, J. F., LAMME, V. A. & ROELFSEMA, P. R. 2007. Boundary assignment in a recurrent network architecture. *Vision Res,* 47**,** 1153-65.

JEURISSEN, D., SELF, M. W. & ROELFSEMA, P. R. 2016. Serial grouping of 2D-image regions with object-based attention in humans. *Elife,* 5.

JIA, X., TANABE, S. & KOHN, A. 2013. gamma and the coordination of spiking activity in early visual cortex. *Neuron,* 77**,** 762-74.

JIA, X. X., SIEGLE, J. H., DURAND, S., HELLER, G., RAMIREZ, T. K., KOCH, C. & OLSEN, S. R. 2022. Multi-regional module-based signal transmission in mouse visual cortex. *Neuron,* 110**,** 1585-+.

JONES, H. E., ANDOLINA, I. M., SHIPP, S. D., ADAMS, D. L., CUDEIRO, J., SALT, T. E. & SILLITO, A. M. 2015. Figure-ground modulation in awake primate thalamus. *Proc Natl Acad Sci U S A,* 112**,** 7085-90.

JUN, J. J., STEINMETZ, N. A., SIEGLE, J. H., DENMAN, D. J., BAUZA, M., BARBARITS, B., LEE, A. K., ANASTASSIOU, C. A., ANDREI, A., AYDIN, C., BARBIC, M., BLANCHE, T. J., BONIN, V., COUTO, J., DUTTA, B., GRATIY, S. L., GUTNISKY, D. A., HAUSSER, M., KARSH, B., LEDOCHOWITSCH, P., LOPEZ, C. M., MITELUT, C., MUSA, S., OKUN, M., PACHITARIU, M., PUTZEYS, J., RICH, P. D., ROSSANT, C., SUN, W. L., SVOBODA, K., CARANDINI, M., HARRIS, K. D., KOCH, C., O'KEEFE, J. & HARRIS, T. D. 2017. Fully integrated silicon probes for high-density recording of neural activity. *Nature,* 551**,** 232-236.

KAPADIA, M. K., ITO, M., GILBERT, C. D. & WESTHEIMER, G. 1995. Improvement in visual sensitivity by changes in local context: parallel studies in human observers and in V1 of alert monkeys. *Neuron,* 15**,** 843-56.

KELLER, A. J., ROTH, M. M. & SCANZIANI, M. 2020. Feedback generates a second receptive field in neurons of the visual cortex. *Nature,* 582**,** 545-549.

KLEINER, M., BRAINARD, D. & PELLI, D. 2007. What's new in Psychtoolbox-3? *Perception,* 36**,** 14-14.

KLINK, P. C., DAGNINO, B., GARIEL-MATHIS, M. A. & ROELFSEMA, P. R. 2017. Distinct Feedforward and Feedback Effects of Microstimulation in Visual Cortex Reveal Neural Mechanisms of Texture Segregation. *Neuron,* 95**,** 209-220 e3.

KNIERIM, J. J. & VAN ESSEN, D. C. 1992. Neuronal responses to static texture patterns in area V1 of the alert macaque monkey. *J Neurophysiol,* 67**,** 961-80.

KO, H. K. & VON DER HEYDT, R. 2018. Figure-ground organization in the visual cortex: does meaning matter? *J Neurophysiol,* 119**,** 160-176.

KOGO, N., STRECHA, C., VAN GOOL, L. & WAGEMANS, J. 2010. Surface construction by a 2-D differentiation-integration process: a neurocomputational model for perceived border ownership, depth, and lightness in Kanizsa figures. *Psychol Rev,* 117**,** 406-39.

KOHN, A. & SMITH, M. A. 2005. Stimulus dependence of neuronal correlation in primary visual cortex of the macaque. *J Neurosci,* 25**,** 3661-73.

KOURTZI, Z. & KANWISHER, N. 2001. Representation of perceived object shape by the human lateral occipital complex. *Science,* 293**,** 1506-9.

LAMME, V. A. 1995. The neurophysiology of figure-ground segregation in primary visual cortex. *J Neurosci,* 15**,** 1605-15.

LAMME, V. A., ZIPSER, K. & SPEKREIJSE, H. 1998. Figure-ground activity in primary visual cortex is suppressed by anesthesia. *Proc Natl Acad Sci U S A,* 95**,** 3263-8.

LAYTON, O. W., MINGOLLA, E. & YAZDANBAKHSH, A. 2012. Dynamic coding of border-ownership in visual cortex. *J Vis,* 12**,** 8.

LEE, T. S., YANG, C. F., ROMERO, R. D. & MUMFORD, D. 2002. Neural activity in early visual cortex reflects behavioral experience and higher-order perceptual saliency. *Nat Neurosci,* 5**,** 589-97.

LI, W., PIECH, V. & GILBERT, C. D. 2006. Contour saliency in primary visual cortex. *Neuron,* 50**,** 951-62.

LI, Y., WANG, T., YANG, Y., DAI, W., WU, Y., LI, L., HAN, C., ZHONG, L., LI, L., WANG, G., DOU, F. & XING, D. 2022. Cascaded normalizations for spatial integration in the primary visual cortex of primates. *Cell Rep,* 40**,** 111221.

LIANG, H., GONG, X., CHEN, M., YAN, Y., LI, W. & GILBERT, C. D. 2017. Interactions between feedback and lateral connections in the primary visual cortex. *Proc Natl Acad Sci U S A,* 114**,** 8637-8642.

LUND, J. S. 1973. Organization of neurons in the visual cortex, area 17, of the monkey (Macaca mulatta). *J Comp Neurol,* 147**,** 455-96.

LUND, J. S. 1988. Anatomical organization of macaque monkey striate visual cortex. *Annu Rev Neurosci,* 11**,** 253-88.

LUND, J. S. & YOSHIOKA, T. 1991. Local circuit neurons of macaque monkey striate cortex: III. Neurons of laminae 4B, 4A, and 3B. *J Comp Neurol,* 311**,** 234-58.

MARCUS, D. S. & VAN ESSEN, D. C. 2002. Scene segmentation and attention in primate cortical areas V1 and V2. *J Neurophysiol,* 88**,** 2648-58.

MARKOV, N. T., VEZOLI, J., CHAMEAU, P., FALCHIER, A., QUILODRAN, R., HUISSOUD, C., LAMY, C., MISERY, P., GIROUD, P., ULLMAN, S., BARONE, P., DEHAY, C., KNOBLAUCH, K. & KENNEDY, H. 2014. Anatomy of hierarchy: feedforward and feedback pathways in macaque visual cortex. *J Comp Neurol,* 522**,** 225-59.

MARTIN, A. B. & VON DER HEYDT, R. 2015. Spike synchrony reveals emergence of proto-objects in visual cortex. *Journal of Neuroscience,* 35**,** 6860-6870.

MATES, S. L. & LUND, J. S. 1983. Neuronal composition and development in lamina 4C of monkey striate cortex. *J Comp Neurol,* 221**,** 60-90.

MEHRANI, P. & TSOTSOS, J. K. 2021. Early recurrence enables figure border ownership. *Vision Res,* 186**,** 23-33.

MELSSEN, W. J. & EPPING, W. J. 1987. Detection and estimation of neural connectivity based on crosscorrelation analysis. *Biol Cybern,* 57**,** 403-14.

MOORE, G. P., SEGUNDO, J. P., PERKEL, D. H. & LEVITAN, H. 1970. Statistical signs of synaptic interaction in neurons. *Biophys J,* 10**,** 876-900.

MULLER, J. R., METHA, A. B., KRAUSKOPF, J. & LENNIE, P. 2003. Local signals from beyond the receptive fields of striate cortical neurons. *J Neurophysiol,* 90**,** 822-31.

NAKAYAMA, K., HE, Z. J. & SHIMOJO, S. 1995. Visual Surface Representation: A Critical Link between Lower-Level and Higher-Level Vision. *In:* KOSSLYN, S. M. & OSHERSON, D. N. (eds.) *An Invitation to Cognitive Science, Volume 2: Visual Cognition.* The MIT Press.

NANDY, A. S., NASSI, J. J. & REYNOLDS, J. H. 2017. Laminar Organization of Attentional Modulation in Macaque Visual Area V4. *Neuron,* 93**,** 235-246.

NASSI, J. J., LOMBER, S. G. & BORN, R. T. 2013. Corticocortical feedback contributes to surround suppression in V1 of the alert primate. *J Neurosci,* 33**,** 8504-17.

NELSON, J. I. & FROST, B. J. 1985. Intracortical facilitation among co-oriented, co-axially aligned simple cells in cat striate cortex. *Exp Brain Res,* 61**,** 54-61.

NELSON, J. I., SALIN, P. A., MUNK, M. H., ARZI, M. & BULLIER, J. 1992. Spatial and temporal coherence in cortico-cortical connections: a cross-correlation study in areas 17 and 18 in the cat. *Vis Neurosci,* 9**,** 21-37.

NICHOLSON, C. & FREEMAN, J. A. 1975. Theory of current source-density analysis and determination of conductivity tensor for anuran cerebellum. *J Neurophysiol,* 38**,** 356-68.

NOTHDURFT, H. C., GALLANT, J. L. & VAN ESSEN, D. C. 1999. Response modulation by texture surround in primate area V1: correlates of "popout" under anesthesia. *Vis Neurosci,* 16**,** 15-34.

NURMINEN, L., MERLIN, S., BIJANZADEH, M., FEDERER, F. & ANGELUCCI, A. 2018. Top-down feedback controls spatial summation and response amplitude in primate visual cortex. *Nat Commun,* 9**,** 2281.

O'HERRON, P. J. & VON DER HEYDT, R. 2009. Short-term memory for figure-ground organization in the visual cortex. *Neuron,* 61**,** 801-809.

O'KUSKY, J. & COLONNIER, M. 1982. A laminar analysis of the number of neurons, glia, and synapses in the adult cortex (area 17) of adult macaque monkeys. *J Comp Neurol,* 210**,** 278-90.

OSTOJIC, S., BRUNEL, N. & HAKIM, V. 2009. How connectivity, background activity, and synaptic properties shape the cross-correlation between spike trains. *J Neurosci,* 29**,** 10234-53.

PACHITARIU, M., SRIDHAR, S., PENNINGTON, J. & STRINGER, C. 2024. Spike sorting with Kilosort4. *Nat Methods,* 21**,** 914-921.

PAK, A., RYU, E., LI, C. & CHUBYKIN, A. A. 2020. Top-Down Feedback Controls the Cortical Representation of Illusory Contours in Mouse Primary Visual Cortex. *J Neurosci,* 40**,** 648-660.

PERKEL, D. H., GERSTEIN, G. L. & MOORE, G. P. 1967. Neuronal spike trains and stochastic point processes. II. Simultaneous spike trains. *Biophys J,* 7**,** 419-40.

PETTINE, W. W., STEINMETZ, N. A. & MOORE, T. 2019. Laminar segregation of sensory coding and behavioral readout in macaque V4. *Proc Natl Acad Sci U S A,* 116**,** 14749-14754.

POLTORATSKI, S. & TONG, F. 2020. Resolving the Spatial Profile of Figure Enhancement in Human V1 through Population Receptive Field Modeling. *J Neurosci,* 40**,** 3292-3303.

POORT, J., RAUDIES, F., WANNIG, A., LAMME, V. A., NEUMANN, H. & ROELFSEMA, P. R. 2012. The role of attention in figure-ground segregation in areas V1 and V4 of the visual cortex. *Neuron,* 75**,** 143-56.

QIU, F. T., SUGIHARA, T. & VON DER HEYDT, R. 2007. Figure-ground mechanisms provide structure for selective attention. *Nature Neuroscience,* 10**,** 1492-1499.

RAMSDEN, B. M., HUNG, C. P. & ROE, A. W. 2001. Real and illusory contour processing in area V1 of the primate: a cortical balancing act. *Cereb Cortex,* 11**,** 648-65.

REID, R. C. & ALONSO, J. M. 1995. Specificity of monosynaptic connections from thalamus to visual cortex. *Nature,* 378**,** 281-4.

ROCKLAND, K. S. & LUND, J. S. 1983. Intrinsic laminar lattice connections in primate visual cortex. *J Comp Neurol,* 216**,** 303-18.

ROCKLAND, K. S. & PANDYA, D. N. 1979. Laminar origins and terminations of cortical connections of the occipital lobe in the rhesus monkey. *Brain Res,* 179**,** 3-20.

ROCKLAND, K. S., SALEEM, K. S. & TANAKA, K. 1994. Divergent feedback connections from areas V4 and TEO in the macaque. *Vis Neurosci,* 11**,** 579-600.

ROCKLAND, K. S. & VIRGA, A. 1989. Terminal arbors of individual "feedback" axons projecting from area V2 to V1 in the macaque monkey: a study using immunohistochemistry of anterogradely transported Phaseolus vulgaris-leucoagglutinin. *J Comp Neurol,* 285**,** 54-72.

ROE, A. W. & TS'O, D. Y. 1999. Specificity of color connectivity between primate V1 and V2. *J Neurophysiol,* 82**,** 2719-30.

ROELFSEMA, P. R. 2006. Cortical algorithms for perceptual grouping. *Annu Rev Neurosci,* 29**,** 203-27.

SAKAI, K. & NISHIMURA, H. 2006. Surrounding suppression and facilitation in the determination of border ownership. *J Cogn Neurosci,* 18**,** 562-79.

SCHWABE, L., OBERMAYER, K., ANGELUCCI, A. & BRESSLOFF, P. C. 2006. The role of feedback in shaping the extra-classical receptive field of cortical neurons: a recurrent network model. *J Neurosci,* 26**,** 9117-29.

SCHWARZ, C. & BOLZ, J. 1991. Functional specificity of a long-range horizontal connection in cat visual cortex: a cross-correlation study. *J Neurosci,* 11**,** 2995-3007.

SELF, M. W., JEURISSEN, D., VAN HAM, A. F., VAN VUGT, B., POORT, J. & ROELFSEMA, P. R. 2019. The Segmentation of Proto-Objects in the Monkey Primary Visual Cortex. *Curr Biol,* 29**,** 1019-1029 e4.

SELF, M. W., VAN KERKOERLE, T., SUPER, H. & ROELFSEMA, P. R. 2013. Distinct roles of the cortical layers of area V1 in figure-ground segregation. *Curr Biol,* 23**,** 2121-9.

SENZAI, Y., FERNANDEZ-RUIZ, A. & BUZSAKI, G. 2019. Layer-Specific Physiological Features and Interlaminar Interactions in the Primary Visual Cortex of the Mouse. *Neuron,* 101**,** 500-513 e5.

SHMUEL, A., KORMAN, M., STERKIN, A., HAREL, M., ULLMAN, S., MALACH, R. & GRINVALD, A. 2005. Retinotopic axis specificity and selective clustering of feedback projections from V2 to V1 in the owl monkey. *J Neurosci,* 25**,** 2117-31.

SIBILLE, J., GEHR, C., BENICHOV, J. I., BALASUBRAMANIAN, H., TEH, K. L., LUPASHINA, T., VALLENTIN, D. & KREMKOW, J. 2022. High-density electrode recordings reveal strong and specific connections between retinal ganglion cells and midbrain neurons. *Nature Communications,* 13.

SIEGLE, J. H., JIA, X., DURAND, S., GALE, S., BENNETT, C., GRADDIS, N., HELLER, G., RAMIREZ, T. K., CHOI, H., LUVIANO, J. A., GROBLEWSKI, P. A., AHMED, R., ARKHIPOV, A., BERNARD, A., BILLEH, Y. N., BROWN, D., BUICE, M. A., CAIN, N., CALDEJON, S., CASAL, L., CHO, A., CHVILICEK, M., COX, T. C., DAI, K., DENMAN, D. J., DE VRIES, S. E. J., DIETZMAN, R., ESPOSITO, L., FARRELL, C., FENG, D., GALBRAITH, J., GARRETT, M., GELFAND, E. C., HANCOCK, N., HARRIS, J. A., HOWARD, R., HU, B., HYTNEN, R., IYER, R., JESSETT, E., JOHNSON, K., KATO, I., KIGGINS, J., LAMBERT, S., LECOQ, J., LEDOCHOWITSCH, P., LEE, J. H., LEON, A., LI, Y., LIANG, E., LONG, F., MACE, K., MELCHIOR, J., MILLMAN, D., MOLLENKOPF, T., NAYAN, C., NG, L., NGO, K., NGUYEN, T., NICOVICH, P. R., NORTH, K., OCKER, G. K., OLLERENSHAW, D., OLIVER, M., PACHITARIU, M., PERKINS, J., REDING, M., REID, D., ROBERTSON, M., RONELLENFITCH, K., SEID, S., SLAUGHTERBECK, C., STOECKLIN, M., SULLIVAN, D., SUTTON, B., SWAPP, J., THOMPSON, C., TURNER, K., WAKEMAN, W., WHITESELL, J. D., WILLIAMS, D., WILLIFORD, A., YOUNG, R., ZENG, H., NAYLOR, S., PHILLIPS, J. W., REID, R. C., MIHALAS, S., OLSEN, S. R. & KOCH, C. 2021. Survey of spiking in the mouse visual system reveals functional hierarchy. *Nature,* 592**,** 86-92.

SILLITO, A. M., GRIEVE, K. L., JONES, H. E., CUDEIRO, J. & DAVIS, J. 1995. Visual cortical mechanisms detecting focal orientation discontinuities. *Nature,* 378**,** 492-6.

SIU, C., BALSOR, J., MERLIN, S., FEDERER, F. & ANGELUCCI, A. 2021. A direct interareal feedback-to-feedforward circuit in primate visual cortex. *Nat Commun,* 12**,** 4911.

SMITH, M. A. & KOHN, A. 2008. Spatial and temporal scales of neuronal correlation in primary visual cortex. *J Neurosci,* 28**,** 12591-603.

SOMOGYI, P. & COWEY, A. 1981. Combined Golgi and electron microscopic study on the synapses formed by double bouquet cells in the visual cortex of the cat and monkey. *J Comp Neurol,* 195**,** 547-66.

STEINMETZ, P. N., ROY, A., FITZGERALD, P. J., HSIAO, S. S., JOHNSON, K. O. & NIEBUR, E. 2000. Attention modulates synchronized neuronal firing in primate somatosensory cortex. *Nature,* 404**,** 187-90.

STETTLER, D. D., DAS, A., BENNETT, J. & GILBERT, C. D. 2002. Lateral connectivity and contextual interactions in macaque primary visual cortex. *Neuron,* 36**,** 739-50.

SUGIHARA, T., QIU, F. T. & VON DER HEYDT, R. 2011. The speed of context integration in the visual cortex. *J Neurophysiol,* 106**,** 374-85.

SUPER, H., ROMEO, A. & KEIL, M. 2010. Feed-forward segmentation of figure-ground and assignment of border-ownership. *PLoS One,* 5**,** e10705.

SUPER, H., SPEKREIJSE, H. & LAMME, V. A. 2001. Two distinct modes of sensory processing observed in monkey primary visual cortex (V1). *Nat Neurosci,* 4**,** 304-10.

SWINDALE, N. V. 1998. Orientation tuning curves: empirical description and estimation of parameters. *Biol Cybern,* 78**,** 45-56.

TOOTELL, R. B., SWITKES, E., SILVERMAN, M. S. & HAMILTON, S. L. 1988. Functional anatomy of macaque striate cortex. II. Retinotopic organization. *J Neurosci,* 8**,** 1531-68.

TRAUTMANN, E. M., HESSE, J. K., STINE, G. M., XIA, R., ZHU, S., O'SHEA, D. J., KARSH, B., COLONELL, J., LANFRANCHI, F. F., VYAS, S., ZIMNIK, A., AMEMATSRO, E., STEINEMANN, N. A., WAGENAAR, D. A., PACHITARIU, M., ANDREI, A., LOPEZ, C. M., O'CALLAGHAN, J., PUTZEYS, J., RADUCANU, B. C., WELKENHUYSEN, M., CHURCHLAND, M., MOORE, T., SHADLEN, M., SHENOY, K., TSAO, D., DUTTA, B. &

HARRIS, T. 2025. Large-scale high-density brain-wide neural recording in nonhuman primates. *Nat Neurosci,* 28**,** 1562-1575.

TREPKA, E. B., ZHU, S. D., XIA, R. B., CHEN, X. M. & MOORE, T. 2022. Functional interactions among neurons within single columns of macaque V1. *Elife,* 11.

TS'O, D. Y., GILBERT, C. D. & WIESEL, T. N. 1986. Relationships between horizontal interactions and functional architecture in cat striate cortex as revealed by cross-correlation analysis. *J Neurosci,* 6**,** 1160-70.

USREY, W. M., REPPAS, J. B. & REID, R. C. 1998. Paired-spike interactions and synaptic efficacy of retinal inputs to the thalamus. *Nature,* 395**,** 384-7.

VAN KERKOERLE, T., SELF, M. W., DAGNINO, B., GARIEL-MATHIS, M. A., POORT, J., VAN DER TOGT, C. & ROELFSEMA, P. R. 2014. Alpha and gamma oscillations characterize feedback and feedforward processing in monkey visual cortex. *Proc Natl Acad Sci U S A,* 111**,** 14332-41.

VAN KERKOERLE, T., SELF, M. W. & ROELFSEMA, P. R. 2017. Layer-specificity in the effects of attention and working memory on activity in primary visual cortex. *Nat Commun,* 8**,** 13804.

VANGENEUGDEN, J., VAN BEEST, E. H., COHEN, M. X., LORTEIJE, J. A. M., MUKHERJEE, S., KIRCHBERGER, L., MONTIJN, J. S., THAMIZHARASU, P., CAMILLO, D., LEVELT, C. N., ROELFSEMA, P. R., SELF, M. W. & HEIMEL, J. A. 2019. Activity in Lateral Visual Areas Contributes to Surround Suppression in Awake Mouse V1. *Curr Biol,* 29**,** 4268-4275 e7.

VON DER HEYDT, R. 2015. Figure-ground organization and the emergence of proto-objects in the visual cortex. *Frontiers in Psychology,* 6**,** 1695.

VON DER HEYDT, R. 2023. Visual cortical processing—From image to object representation. *Frontiers in Computer Science,* 5.

VON DER HEYDT, R., PETERHANS, E. & BAUMGARTNER, G. 1984. Illusory contours and cortical neuron responses. *Science,* 224**,** 1260-2.

WAGATSUMA, N., HU, B., VON DER HEYDT, R. & NIEBUR, E. 2021. Analysis of spiking synchrony in visual cortex reveals distinct types of top-down modulation signals for spatial and object-based attention. *PLoS Comput Biol,* 17**,** e1008829.

WALKER, G. A., OHZAWA, I. & FREEMAN, R. D. 1999. Asymmetric suppression outside the classical receptive field of the visual cortex. *J Neurosci,* 19**,** 10536-53.

WEBB, B. S., TINSLEY, C. J., BARRACLOUGH, N. E., PARKER, A. & DERRINGTON, A. M. 2003. Gain control from beyond the classical receptive field in primate primary visual cortex. *Vis Neurosci,* 20**,** 221-30.

WILLIFORD, J. R. & VON DER HEYDT, R. 2016. Figure-Ground Organization in Visual Cortex for Natural Scenes. *eNeuro,* 3.

WISER, A. K. & CALLAWAY, E. M. 1996. Contributions of individual layer 6 pyramidal neurons to local circuitry in macaque primary visual cortex. *J Neurosci,* 16**,** 2724-39.

XU, X., OLIVAS, N. D., IKRAR, T., PENG, T., HOLMES, T. C., NIE, Q. & SHI, Y. 2016. Primary visual cortex shows laminar-specific and balanced circuit organization of excitatory and inhibitory synaptic connectivity. *J Physiol,* 594**,** 1891-910.

YABUTA, N. H. & CALLAWAY, E. M. 1998. Functional streams and local connections of layer 4C neurons in primary visual cortex of the macaque monkey. *J Neurosci,* 18**,** 9489-99.

YAN, Y., ZHAOPING, L. & LI, W. 2018. Bottom-up saliency and top-down learning in the primary visual cortex of monkeys. *Proc Natl Acad Sci U S A,* 115**,** 10499-10504.

YOSHIOKA, T., LEVITT, J. B. & LUND, J. S. 1994. Independence and merger of thalamocortical channels within macaque monkey primary visual cortex: anatomy of interlaminar projections. *Vis Neurosci,* 11**,** 467-89.

ZARELLA, M. D. & TS'O, D. Y. 2016. Cue combination encoding via contextual modulation of V1 and V2 neurons. *Eye Brain,* 8**,** 177-193.

ZHANG, N. R. & VON DER HEYDT, R. 2010. Analysis of the context integration mechanisms underlying figure-ground organization in the visual cortex. *Journal of Neuroscience,* 30**,** 6482-6496.

ZHANG, S., XU, M., KAMIGAKI, T., HOANG DO, J. P., CHANG, W. C., JENVAY, S., MIYAMICHI, K., LUO, L. & DAN, Y. 2014. Selective attention. Long-range and local circuits for top-down modulation of visual cortex processing. *Science,* 345**,** 660-5.

ZHAOPING, L. 2005. Border ownership from intracortical interactions in visual area v2. *Neuron,* 47**,** 143-53.

ZHOU, H., FRIEDMAN, H. S. & VON DER HEYDT, R. 2000. Coding of border ownership in monkey visual cortex. *J Neurosci,* 20**,** 6594-611.

ZHU, S., XIA, R., CHEN, X. & MOORE, T. 2024. Comparison of orientation encoding across layers within single columns of primate V1 revealed by high-density recordings. *Front Neural Circuits,* 18**,** 1399571.

ZHU, S. D., ZHANG, L. A. & VON DER HEYDT, R. 2020. Searching for object pointers in the visual cortex. *Journal of Neurophysiology,* 123**,** 1979-1994.

ZIPSER, K., LAMME, V. A. & SCHILLER, P. H. 1996. Contextual modulation in primary visual cortex. *J Neurosci,* 16**,** 7376-89.

Figures and legend

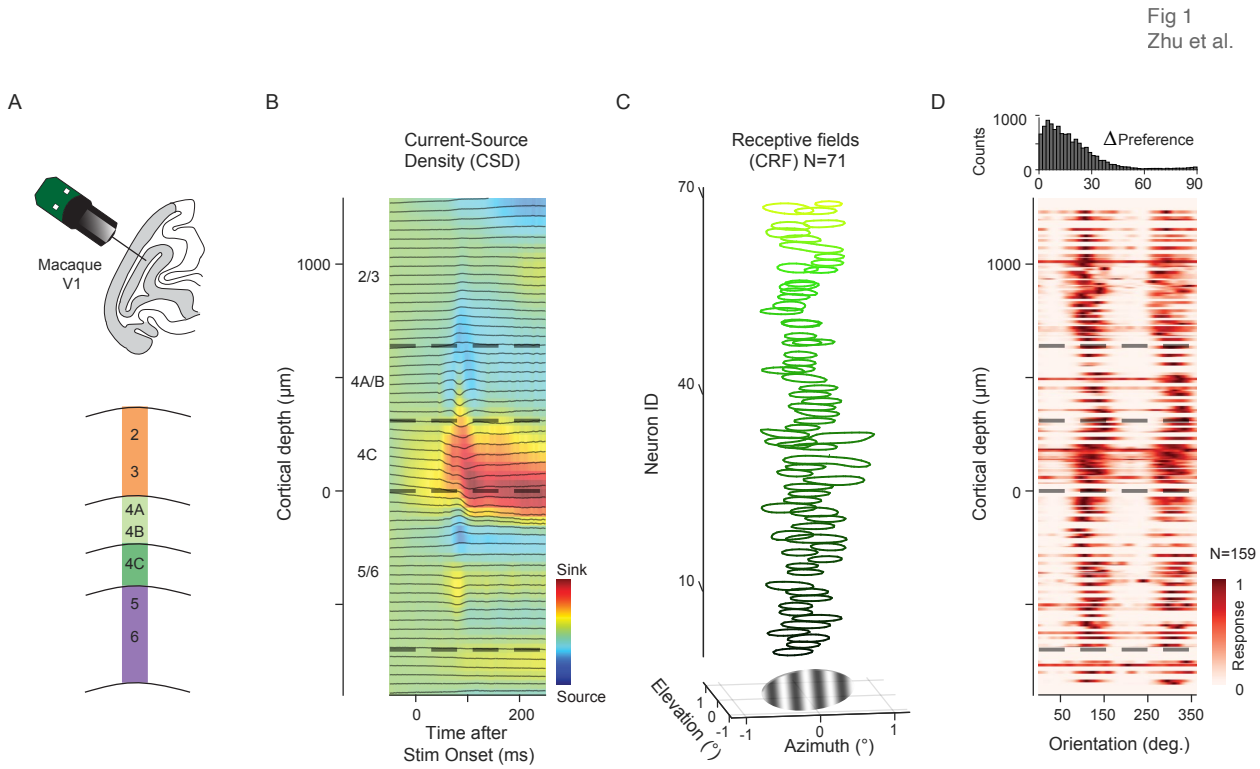

Figure 1. Classical receptive field (CRF) stimulation in single V1 columns.
(A) Neuropixels probe (384 channels/3.84mm) penetrations made into the lateral surface or underlying calcarine sulcus of macaque V1. Bottom: Diagram of designated laminar compartments. (B) Current-Source density (CSD) profile from an example recording session (M1, *pen1*), showing the early current sink (red) indicative of layer 4C. Laminar compartment boundaries (dashed lines) were determined using histological data and the CSD profile. (C) Top: 71 well-defined classical receptive fields (CRF) vertically stacked along the cortical depth, mapped with a 10 x 10 array (4 x 4 dva) of probe stimuli (gratings, 0.4 dva in diameter). Bottom: Drifting Gabor grating (1.5 dva in diameter) used for CRF stimulation, positioned within the joint receptive fields of recorded neurons. Zero (x, y) denotes the center of the CRF population. (D) Heatmap of visual responses from 159 neurons to 36 drift directions of Gabor gratings, vertically stacked along cortical depth (M1, *pen1*). Top: Distribution of differences in preferred orientation for all pairwise combinations of neurons.

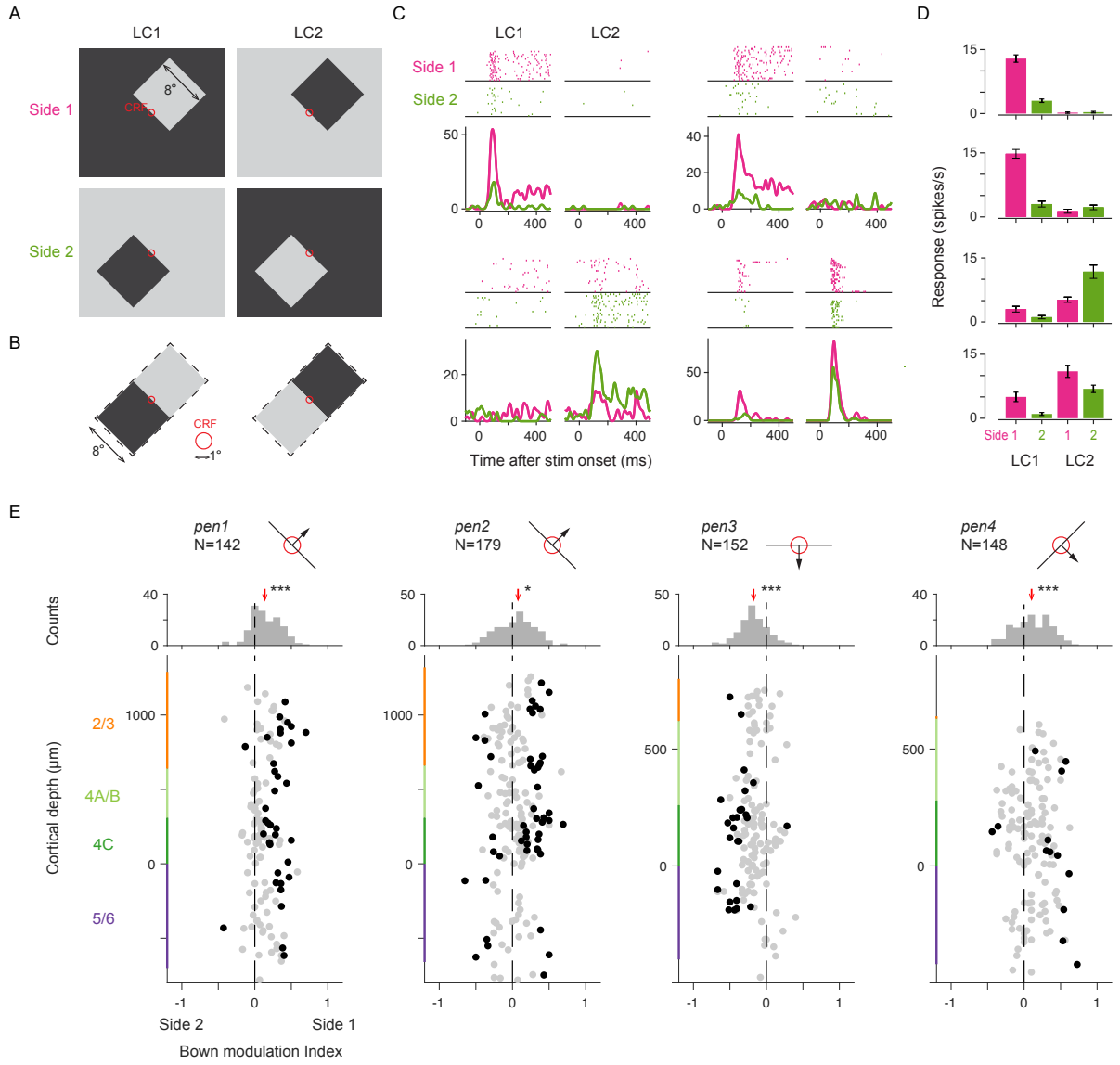

Figure 2. Nonclassical receptive field (nCRF) stimulation and border ownership.
(A) Border ownership test stimuli for nCRF stimulation. Stimuli consisted of uniformly white or black objects (8º squares) on black or white backgrounds, respectively. One border of the object fell within the CRFs (red circle) of the recorded neurons, with orientation varying in 45º steps. Within the CRF, depending on local contrast polarity (LC), the border could either be a dark-light edge (LC1, Left column) or a light-dark edge (LC2, Right column). For the same LC condition, the border within the CRF could be the bottom-left edge (Side 1, top row) or top-right edge (Side 2, bottom row) of the object. (B) Enlarged view of stimulus configuration within the CRF, showing identical stimulus regions between Side 1 and Side 2 for each LC condition (8 x 16 dva). (C) Four example B_{own} neurons recorded from V1. For each neuron, dot raster plots (top) and instantaneous firing rates (bottom) show responses to the four stimulus conditions depicted in (A), respectively. Magenta represents Side 1; green represents Side 2. (D) Bar plots showing the mean spike rates of the four neurons across the four stimulus conditions. (E) Top: Cartoon depicting the preferred border orientation for each of the four recording sessions (*pen*1-4). Arrows indicate the preferred side of objects relative to the border in the CRF. Bottom: B_{own} modulation index for each neuron plotted at its recorded cortical depth across the recordings. Color bars on the ordinate represent laminar compartments. Black dots denote statistically significant B_{own} neurons, determined by ANOVA with object side and local contrast as factors ($p < 0.05$). Middle: Marginal distribution of the B_{own} modulation index, red arrows indicating the population median. *$p < 0.05$; ***$p < 10^{-5}$.

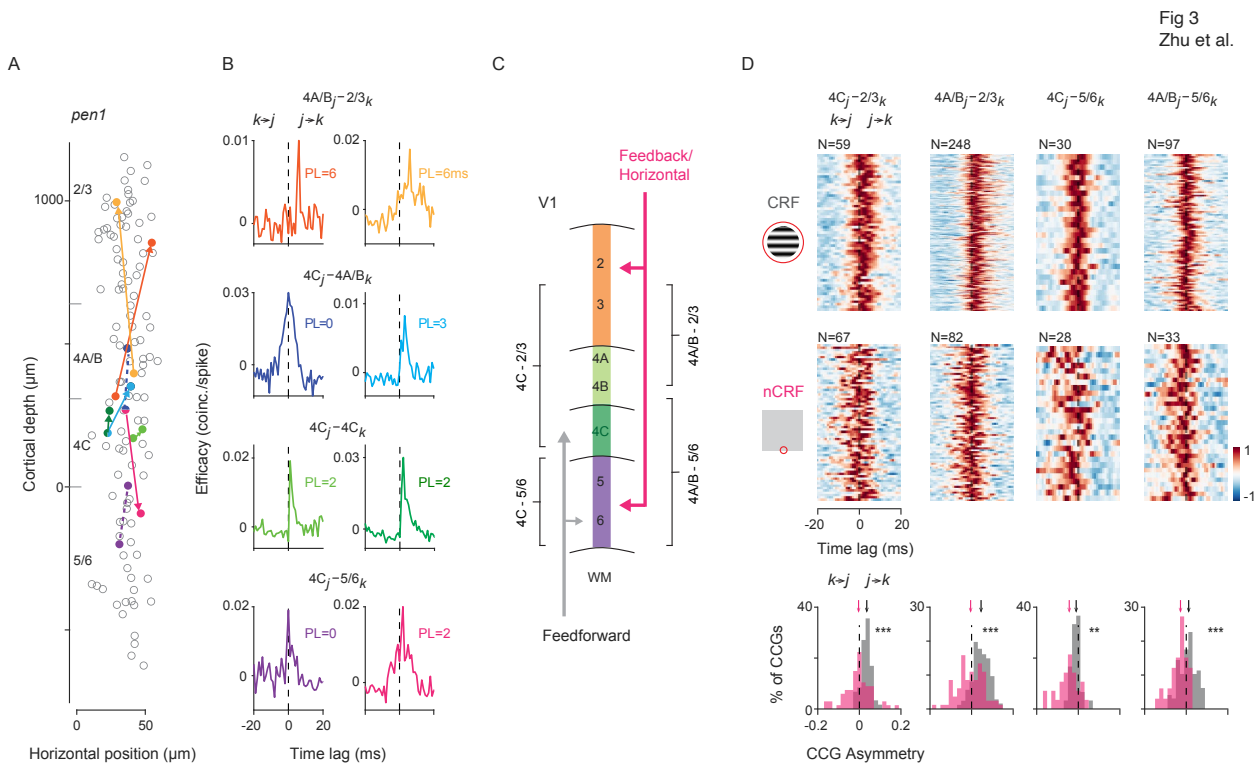

Figure 3. Interlaminar cross-correlations during CRF and nCRF stimulation.
(A) Example recording (M1, *pen1*) showing 159 visually responsive neurons (circles) recorded simultaneously during CRF stimulation, plotted at their relative cortical depth. The abscissa is magnified for visualization. Also shown are eight example neuronal pairs with significant CCGs during CRF stimulation. Neuronal pairs with zero-time lag CCGs are connected by dashed lines, while pairs with nonzero-time lag CCGs are connected by arrowed lines, with the arrow pointing to the lagging neuron. (B) Eight corresponding CCGs from (A). Neuronal pairs are separated by their laminar compartment combinations. The reference neuron (1st neuron in the CCG function) is designated as *j*, and the target neuron as *k*. PL (peak lag, ms) is defined as the relative time delay in peak correlation between the two spike trains. (C) Diagram illustrating feedforward and feedback (and horizontal) projections within the designated laminar compartments. Feedforward inputs arrive within laminar compartments 4C and 6, while feedback (and horizontal) projections principally target superficial and deep layers. (D) Heatmap of all significant CCGs during either CRF stimulation (Gabor gratings, top row) or nCRF stimulation (border ownership, middle row), for the four key interlaminar combinations (columns), calculated from one example recording (M1, *pen1*). Individual CCGs are normalized by their absolute maximum for visualization, and different CCGs are vertically stacked. Bottom row: Distribution of CCG asymmetry for each of the four key interlaminar compartments as in (A), across CRF stimulation (gray) and nCRF stimulation (magenta). Arrows indicate the population median. $^{**}p < 0.002$; $^{***}p < 10^{-5}$.

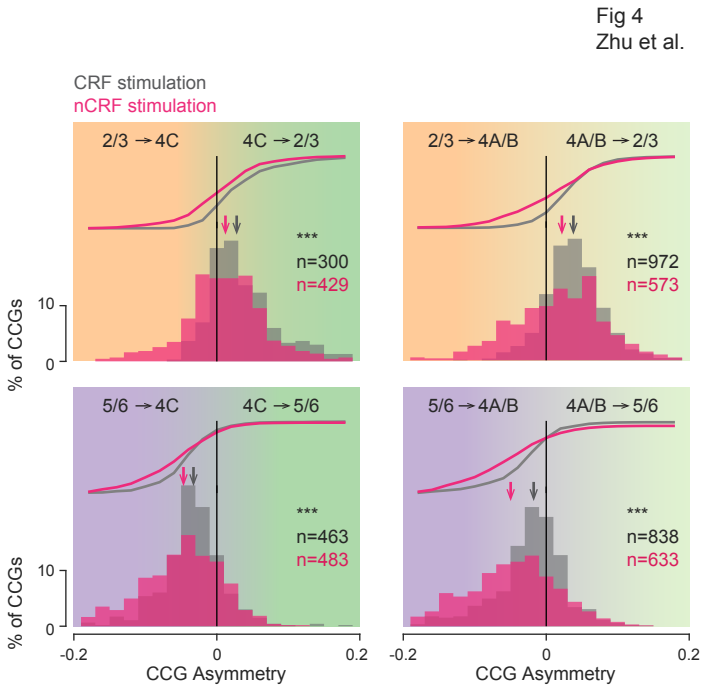

Figure 4. Comparison of interlaminar CCG asymmetries during CRF and nCRF stimulation. Combined dataset for each of the four key interlaminar combinations. Histograms and cumulative distributions of asymmetry for all significant CCGs during CRF (gray) and nCRF (magenta) stimulation. Arrows indicate the population median. ***$p < 10^{-5}$.

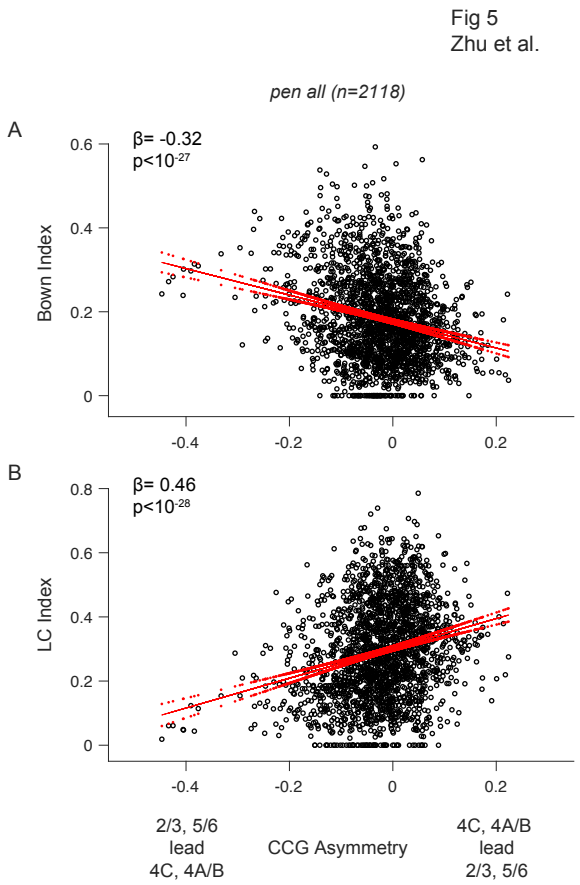

Figure 5. Dependence of nCRF modulation on interlaminar signal flow.
(A) Scatter plot of the B_{own} modulation index versus CCG asymmetry for all significant CCGs, aggregated across the four key interlaminar combinations and all recording sessions. CCG asymmetries were calculated during nCRF stimulation. The geometric mean of the B_{own} index for each neuronal pair was used. Red lines denote the fitted regression line and the 95% confidence interval in linear regression. (B) Similar to (A), but using the local contrast (LC) index instead of the B_{own} index. The LC index was calculated as the difference in neuronal responses to borders with opposite contrast polarities, normalized by the maximum response.

Supplementary figures and legends

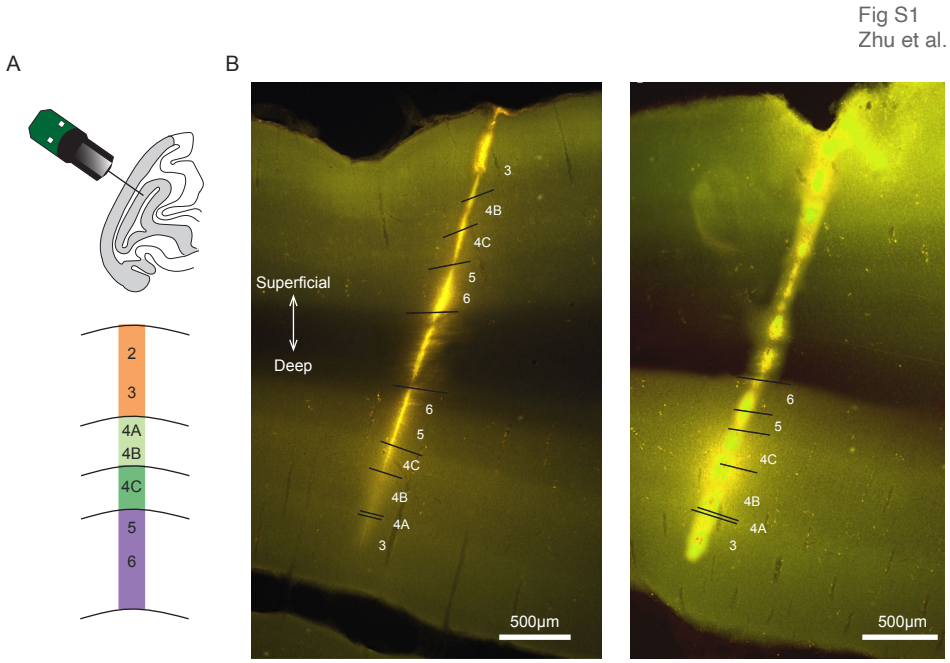

Supplementary Figure S1. Histological data for Neuropixels recordings in macaque V1.
(A) Neuropixels probe (384 channels/3.84mm) penetrations made into the lateral surface or underlying calcarine sulcus of macaque V1. Bottom: Diagram of designated laminar compartments. (B) Histological reconstruction of probe tracks based on DiI derivative staining for two example recordings (*pen3-4*). Here, Neuropixels probes passed through the lateral surface and reached the calcarine sulcus of V1. Only neurons in the calcarine V1 from these two recordings were tested and included in the analysis. Designated boundaries are shown. Scale bar, 500 µm.

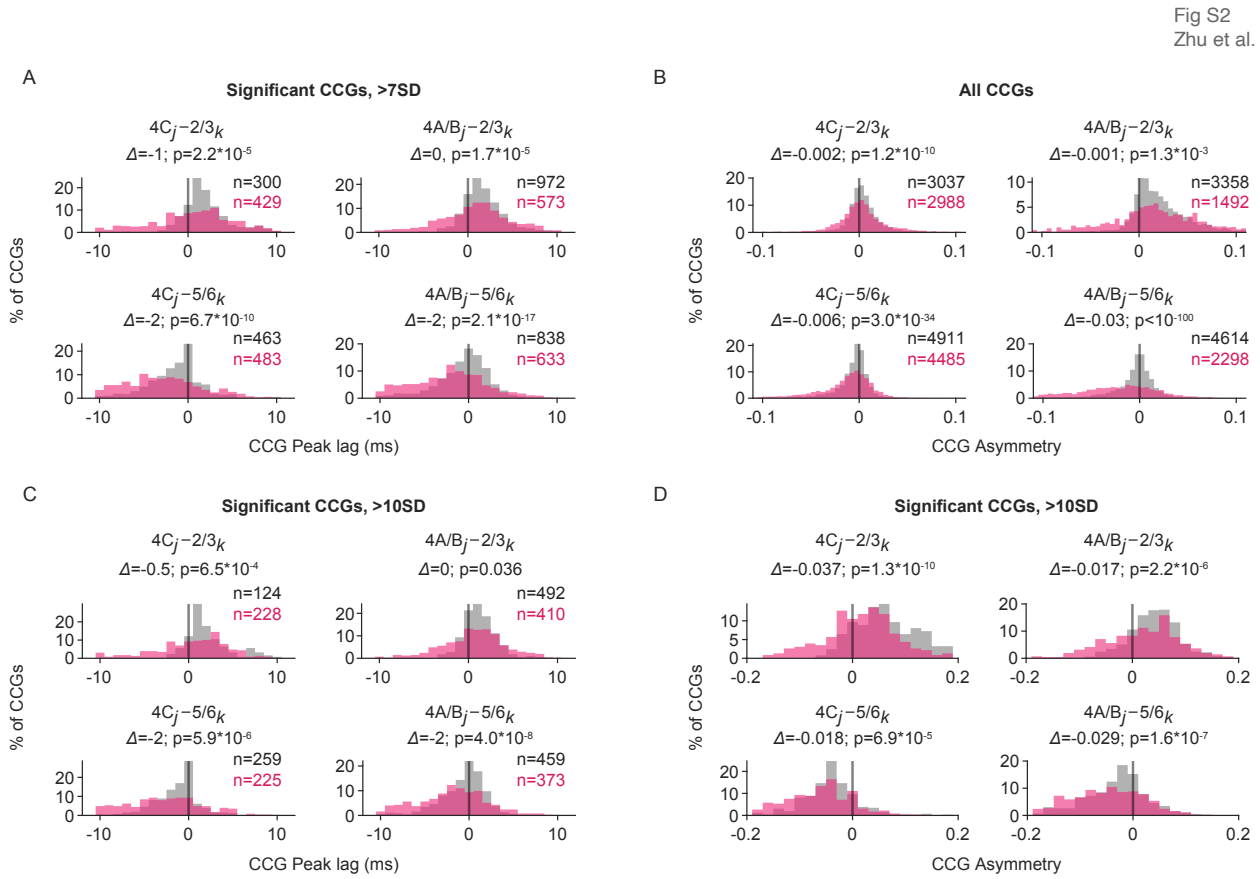

Supplementary Figure S2. Comparison of interlaminar cross-correlations during CRF and nCRF stimulation under different CCG criteria.

(A) Histogram distributions of CCG peak lags for each of the four key interlaminar combinations in the combined dataset during CRF (gray) and nCRF (magenta) stimulation. The shift (Δ) in median CCG peak lags during nCRF stimulation relative to CRF stimulation is shown. Significant CCGs are defined as those with peaks exceeding 7 SD above the noise level (flank). (B) Similar to (A), but comparing CCG asymmetry across all CCGs, including both significant and non-significant ones. (C) Comparison of CCG peak lags using a stricter criterion, where significant CCGs are defined as those with peaks exceeding 10 SD above the noise level (flank). (D) Comparison of CCG asymmetry using the stricter criterion of 10 SD.